Cell-to-cell variation in defective virus expression and effects on host responses during influenza virus infection

Chang Wang[1], Christian V. Forst[2], Tsui-wen Chou[1], Adam Geber[1], Minghui Wang[2], Wissam Hamou[2], Melissa Smith[2], Robert Sebra[2], Bin Zhang[2], Bin Zhou[1,#], and Elodie Ghedin[1,3*]

[1]Center for Genomics and Systems Biology, Department of Biology, New York University

[2]Mount Sinai Center for Transformative Disease Modeling, Department of Genetics and Genomic Sciences, Icahn Institute of Genomics and Multiscale Biology, Icahn School of Medicine at Mount Sinai

[3]College of Global Public Health, New York University, New York, New York

[#]Current address: Bin Zhou, nmb7@cdc.gov, Influenza Division, National Center for Immunization and Respiratory Diseases, Centers for Disease Control and Prevention, Atlanta, Georgia

* Corresponding author

E-mail: elodie.ghedin@nyu.edu

ABSTRACT

Virus and host factors contribute to cell-to-cell variation in viral infections and determine the outcome of the overall infection. However, the extent of the variability at the single cell level and how it impacts virus-host interactions at a systems level are not well understood. To characterize the dynamics of viral transcription and host responses, we used single-cell RNA sequencing to quantify at multiple time points the host and viral transcriptomes of human A549 cells and primary bronchial epithelial cells infected with influenza A virus. We observed substantial variability of viral transcription between cells, including the accumulation of defective viral genomes (DVGs) that impact viral replication. We show a correlation between DVGs and viral-induced variation of the host transcriptional program and an association between differential induction of innate immune response genes and attenuated viral transcription in subpopulations of cells. These observations at the single cell level improve our understanding of the complex virus-host interplay during influenza infection.

AUTHOR SUMMARY

Defective influenza virus particles, which are products of error-prone viral replication, carry incomplete versions of the genome and can interfere with the replication of competent viruses. These defective genomes are thought to modulate disease severity and pathogenicity of the influenza infection. Different defective viral genomes can have different interfering abilities, and introduce another source of variation across a heterogeneous cell population. Evaluating the impact of defective virus genomes on host cell responses cannot be fully resolved at the population level, requiring single cell transcriptional profiling. Here we characterized virus and host transcriptomes in influenza-infected cells, including that of defective viruses that arise during influenza A virus infection. We profiled single cell transcriptional landscapes over the course of the infection and established an association between defective virus transcription and host responses. We identified dominant defective viral genome species and validated their interfering and immunostimulatory functions *in vitro*. This study demonstrates the intricate effects of defective viral genomes on host transcriptional responses and highlights the importance of capturing host-virus interactions at the single-cell level.

INTRODUCTION

The productivity of viral replication at the cell population level is determined by cell-to-cell variation in viral infection [1]. The genetically diverse nature of RNA viruses and the heterogeneity of host cell states contribute to this inter-cell variability, which can impact therapeutic applications [2, 3]. Although previous studies of cell-to-cell variation during viral infection have mainly centered on non-segmented viruses such as poliovirus [2, 4], vesicular stomatitis virus (VSV) [5, 6], or dengue (DENV) and zika (ZIKV) viruses [7], heterogeneity across cells may be further complicated for viruses with a segmented genome, such as influenza A virus (IAV). IAV-infected cells display substantial cell-to-cell variation as it pertains to relative abundance of different viral genome segments [1, 8], transcripts [9], and their encoded proteins [10], which can result in non-productive infection in a large fraction of cells.

Defective interfering (DI) particles readily generated during successive high multiplicity of infection (MOI) in cell culture passages [11-14] and observed in natural infections [15, 16] are likely by-products of an inefficient IAV replication process and have a significant effect on productive infection. DI viruses have incomplete viral genomes with large internal deletions and they possess the ability to interfere with the replication of infectious viruses. Because DIs diminish the productivity of infectious progenies and could impact disease outcome, they are of great interest for therapeutic and prophylactic purposes (reviewed in [17]). A specific influenza DI (i.e., DI244) was shown to effectively provide prophylactic and therapeutic protection against IAV infection in mice [18]. One of the ways influenza DIs are thought to modulate viral infections is through interaction with a cytosolic pathogen-recognition receptor (PRR), RIG-I, essential for interferon (IFN) induction [19]. Besides enhanced IFN induction during infection with DI-rich influenza virus populations observed *in vitro* and *in vivo*, it has been assumed that DI virus could also compete with standard virus for cellular resources (reviewed in [17, 20]).

75 While diverse DI viruses can arise during IAV infection [21], the emergence and accumulation of
76 distinct DIs, as well as other defective virus genomes (DVGs), has not been characterized at a
77 single cell resolution, although the diversity of DIs present could be contributing to the observed
78 cell-to-cell variation in host transcription.
79
80 We probed viral and host transcriptomes simultaneously in the same cells using single-cell
81 RNA-seq to monitor host-virus interactions in cultured cells over the course of the infection. This
82 data established a temporal association between the level of viral transcription and the
83 alteration of the host transcriptome, and characterized the diversity and accumulation of DVG
84 transcripts.
85

RESULTS

Cell-to-cell variation in virus gene expression.

To determine how both the viral and host cell transcriptional programs relate to each other over the course of an influenza infection, we infected two cell types—the adenocarcinomic human alveolar basal epithelial A549 cell line and human primary bronchial epithelial cells HBEpC—at high multiplicity of Infection (MOI) with A/Puerto Rico/8/34(H1N1) (PR8) and performed single cell and bulk RNA-seq expression analyses. A high MOI infection ensures that virtually all the cells can be rapidly infected, promotes the accumulation of DVGs, and consequently enables the characterization of both host response and DVG diversity. We first determined the percentage of reads that uniquely aligned to viral genes from the total number of mapped reads to obtain the relative abundance of virus transcripts within cells at each time point. Similar to what has been observed at early stages of infection during a low MOI infection of IAV [9], the relative abundance of viral transcripts was heterogeneous across cells from both cell types, with 0 to 70% of the total reads in each cell being derived from viral transcripts, with the relative abundance of these transcripts increasing over time (**Supplementary Fig. 1a**). The same trend was also seen when analyzing segment-specific viral transcripts within individual cells over the course of the infection (**Supplementary Fig. 1b**).

Heterogeneity of defective virus segment expression across the cell population.

Since DVGs are known to accumulate in cell culture and can serve as templates for transcription, we characterized their abundance and diversity by examining gap-spanning reads in the sequencing data. As the large majority of DVGs in IAV originate from the polymerase segments (i.e., PB2, PB1, and PA) [15], we focused on the detection of DVG transcripts derived from those segments. We collected the reads with large internal deletions spanning ≥1000 nucleotides (nt) (**Fig. 1a**) and identified the junction coordinates of these gap-spanning reads. We observed a diverse pool of DVG transcripts, including some shared with the viral segments

(vRNA) from the PR8 stock (**Supplementary Fig. 2-4**). The sizes of the majority of these DVG transcripts are estimated to be between 300nt and 1000nt.

To quantify the relative abundance of DVGs identified, we calculated the frequency of each unique DVG transcript type (determined by 5' / 3' gap coordinates) across single cells and the ratio of these to non-gap-spanning transcripts derived from the corresponding viral segments (i.e., DVG/FL ratio). The DVG/FL ratio, which represents the ratio of DVG transcripts to that of the full-length (FL) transcripts, derived from a given polymerase segment increased significantly between the early (6hpi) and late (24hpi) stages of the infection ($p < 2.2 \times 10^{-16}$) and displayed a high level of heterogeneity across single cells from both cell types (**Supplementary Fig. 5**). Interestingly, the junction sites aggregated in specific genomic regions, as they systematically occurred in a high percentage of cells. We identified two predominant types of DVG transcripts corresponding to PB2 and PB1 defective segments (**Fig. 1b-c** and **Supplementary Fig. 6-7**). These same DVG transcripts were present in the stock, increased in prevalence over the course of the infection, and were conserved in different cell types and at different MOIs, (**Supplementary Fig. 8-9**) indicating likely carryover from the stock virus rather than *de novo* formation in each new cell type. For PA, one particular DVG type that was present in the stock was found in A549 and MDCK cells at different MOIs, but not in HBEpC cells. Its prevalence was also much lower than for PB2 and PB1 DVGs (**Supplementary Fig. 10-11**). The dominant DVG PB2 and PB1 transcripts derived from corresponding defective segments in both the stock and the infected cells showed stable relative abundance across individual cells over the course of the infection, suggesting the persistence of the defective viral segments.

To determine if any of the inferred defective polymerase segments could lead to the generation of defective interfering particles (DIs), we tested their interfering potential experimentally. We generated clonal PB8-DI162 and PR8-DI222 viruses carrying the deletion sites in the PB2

138 segment identified as those in two dominant PB2-DVG species and then co-infected each of the
139 DI viruses with PR8 wild-type (WT) virus in A549 cells. Both PR8-DI162 and PR8-DI222 viruses
140 can inhibit the productivity of WT virus, comparable to the interfering ability of PR8-DI244 that is
141 known to be an effective DI [18] (**Fig. 1d**). This confirmed the interfering ability of the two types
142 of defective PB2 segments identified in the single cell data.
143
144 **Differential expression of host genes linked to defective viral genomes**
145 Viral infection can trigger massive changes in the host transcriptional program, including the
146 activation of the interferon (IFN) response. Since the induction of IFNs is also subject to cell-to-
147 cell variation [22], we first evaluated the expression frequency of type I (i.e., IFN beta) and III
148 (i.e., IFN lambda) IFNs to determine the extent of the variation during infection. While these
149 were significantly differentially expressed over the course of the infection at the population level,
150 as measured by bulk RNA-seq (**Fig. 2a**), the expression of IFNs was only detected in less than
151 3% of cells until the late stage of infection, although this proportion increased over time (**Fig. 2b**
152 and **Fig. 2c**). The same expression profile was observed for a number of IFN-stimulated genes
153 (ISGs), such as *RSAD2*, *CXCL10*, *GBP4*, *GBP5*, *IDO1*, and *CH25H* in A549 cells, and *IFI44L*,
154 *CMPK2*, *IFIT1*, *BST2*, *OASL*, and *XAF1* in HBEpC (**Fig. 2**). In silico pooling of the single cell
155 data to mimic the population level measurement resembles the bulk RNA-seq data, thus
156 excluding the possibility of substantial technical limitation of single-cell RNA-seq
157 (**Supplementary Fig. 12**).
158
159 To evaluate cell-to-cell variation in the host response manifested by the alteration in the host
160 transcriptome following IAV infection, we performed un-supervised cell clustering using the host
161 transcriptional profile. We then annotated single cells in each subpopulation with information
162 about the relative abundance of viral transcripts and the DVG/FL ratio. We detected significant
163 effects of viral transcription on the host transcriptome, as cells with a high level of viral

transcription formed a separate cluster by 12hpi in both cell types (**Fig. 3a** and **Fig. 3b**), while the other cells clustered primarily according to their cell cycle stage (**Supplementary Fig. 13a** and **Supplementary Fig. 13b**). Consistent with previous reports on G0/G1 cell-cycle arrest [23, 24], the most drastic alteration in cell-cycle distribution was observed in A549 cells at 24hpi, when the host gene expression pattern varied along a gradient based on the relative abundance of viral transcripts (**Fig. 3a**).

To characterize the host genes driving the changes associated with viral transcription, we assessed the over-representation of Gene Ontology (GO) terms associated with differentially expressed genes in each subpopulation of A549 and HBEpC cells compared to the rest of the cells at 24hpi. In two subpopulations of A549 cells with a high relative abundance of viral transcripts (clusters 0 and 1 in **Fig. 4a**), there is enrichment of genes involved in transcription, RNA processing, translation, SRP-dependent co-translational protein targeting to the membrane, mitochondrial electron transport and ATP synthesis (**Fig. 4a**). These GO terms are also associated with genes highly expressed in HBEpC cells with the highest level of viral transcription at 24hpi (cluster 3 in **Fig. 4b**; $p < 2.2 \times 10^{-16}$ compared to the other clusters). In contrast, genes involved in antiviral responses, such as the type I IFN signaling pathway and the negative regulation of viral genome replication, are over-expressed in the other two subpopulations of A549 cells with a similar or severely reduced relative abundance of viral transcripts (clusters 3 and 2, respectively in **Fig. 4a**). However, some antiviral genes are differentially induced in cells with different levels of viral transcription. For example, type I and III IFNs, as well as a subset of ISGs, are over-expressed in cluster 3, and another subset of ISGs are over-expressed in cluster 2. In HBEpC cells, the antiviral responses, such as the type I IFN signaling pathway, are primarily observed in a cluster (cluster 2 in **Fig. 4b**) that has a low level of viral transcription (**Fig 3b** at 24hpi**)** and mostly comprised of cells in the G0/G1 phase (**Supplementary Fig. 13b** at 24hpi).

Since DVGs are known to play an important role in IFN induction and inhibition of viral replication (reviewed in [20]), we determined whether the accumulation of DVGs was associated with attenuated viral transcription and induction of innate immune antiviral response genes. We observed an inverse trend between the relative abundance of viral transcripts and the accumulation of defective PB2 and PB1 segments at the mid (12hpi) and late (24hpi) stages of infection (**Fig. 5a-f**). The cluster of cells with the highest level of viral transcription (cluster 1 of A549 cells at 12hpi in **Fig. 5a** and cluster 3 of HBEpC cells at 24hpi in **Fig. 5b**) has the lowest level of PB2 and PB1 DVG/FL ratios (**Fig. 5c-d**; $p < 2.2 \times 10^{-16}$ comparing PB2 and PB1 DVG/FL ratios in cluster 1 of A549 cells or cluster 3 of HBEpC cells against the other clusters). Similarly, in A549 cells at 24 hpi, we see the lowest level of viral transcription in cells (cluster 2 in **Fig. 5e**) that have a higher level of PB2 DVG/FL ratios (cluster 2 in **Fig. 5f**; $p < 2.2 \times 10^{-16}$ compared to clusters 0 and 1) and the highest level of PB1 DVG/FL ratios ($p = 1.943 \times 10^{-9}$ comparing cluster 2 against the other clusters). Moreover, given the fact that the innate immune response genes are highly expressed in cells with an elevated relative abundance of both DVG PB2 and PB1 transcripts (cluster 2 of A549 cells at 24 hpi in **Fig. 5f**), or just DVG PB2 transcripts (cluster 3 in **Fig. 5f**; $p = 4.036 \times 10^{-11}$ compared to clusters 0 and 1), it suggests an association between the accumulation of DVGs and the strong stimulation of the innate immune response compared to the rest of the cells in the same population, where secreted IFNs are accessible to all the cells. Notably, the DVG PB2 transcripts carrying the same deletion sites as for PR8-DI222 were highly abundant in the cluster of cells with the lowest level of viral transcription (cluster 2 of A549 cells at 24 hpi in **Fig. 5g**; $p < 2.2 \times 10^{-16}$ compared to the other clusters), while the other DVG PB2 transcripts corresponding to PR8-DI162 were highly abundant in both cluster 2 and cluster 3 (**Fig. 5g**; $p = 2.067 \times 10^{-10}$ and $p = 0.001241$, respectively, compared to clusters 0 and 1), suggesting a potential difference in the induction of innate immune response genes by different DVG species. We did not detect a difference in the

relative abundance of defective PA segments among cells with different levels of viral transcription (**Supplementary Fig. 14**).

To further understand how transcriptional activity is coordinated in clusters of cells that confront different levels of viral stimuli, including DVGs, we performed gene co-expression network analyses using multiscale embedded gene co-expression network analysis (MEGENA) [25]. This was done independently within each cluster of A549 and HBEpC cells collected at 24 hpi to identify modules of co-expressed genes representing coherent functional pathways. The relevance of a module to viral infection in terms of the host response and viral replication was evaluated by the enrichment of differentially expressed disease gene (DEDG) signatures compared to the mock-infected cells and by correlating with the relative abundance of viral transcripts and DVG/FL ratios. Consistent with the processes identified in the GO over-representation test (**Fig. 4**), those related to the host cell cycle and viral life cycle, especially at the late stage of viral replication, including protein synthesis and transport, are enriched in the top-ranked modules identified in the clusters of A549 cells with a high level of viral transcription (**Fig. 6a, Supplementary Fig. 15a and 15b**). Conversely, the host innate immune response (e.g., type I IFN signaling pathway) was primarily associated with several top-ranked modules in cells with the lowest level of viral transcription (cluster 2 of A549 cells at 24hpi in **Fig. 6b**) and in high IFN-producing cells with a high level of viral transcription (cluster 3 of A549 cells at 24hpi in **Fig. 6a**). For example, module M100 in cluster 2 of A549 cells had key regulators involved in the innate antiviral response that were significantly up-regulated, compared to the mock-infected cells, including *ISG20, RNF213, IFI35, STAT1*, and *RBCK1* (**Fig. 6b**) and showed a strong negative correlation with the level of viral transcription ($\rho = -0.26$, $p = 2.9 \times 10^{-5}$); and Module M3 in cluster 3 of A549 cells had key regulators including *IFNL1* and some ISGs (e.g., *OASL* and *ISG15*) (**Fig. 6a**). A top-ranked module associated with the type I IFN signaling pathway was also observed in cluster 1 of A549 cells with a high level of viral transcription (M13 in

242 **Supplementary Fig. 15b**) and it shared a common key regulator, *ISG15*, with the other IFN
243 signaling modules detected in clusters 2 and 3 (**Supplementary Fig. 15c and Fig. 6a)**.
244 However, a top-ranked module (M234 in **Supplementary Fig. 15c**) enriched for the chemokine-
245 mediated signaling pathway, particularly the regulation of granulocytes (e.g., neutrophils)
246 chemotaxis, was observed in another cluster of A549 cells with a high level of viral transcription
247 (i.e., cluster 0). Nonetheless, in HBEpC cells, top-ranked modules enriched for type I IFN
248 signaling genes were detected in all four clusters of cells with different levels of viral
249 transcription (**Fig. 6c** and **Supplementary Fig. 16**). These modules in three clusters of HBEpC
250 cells with a low level of viral transcription (i.e., clusters 0, 1, and 2 in **Fig. 6c** and
251 **Supplementary Fig. 16**), including Module M227 in cluster 2 of HBEpC cells with a significant
252 positive correlation with the level of viral transcription ($\rho = 0.10$, $p = 0.021$) (**Fig. 6c**), also shared
253 the same key regulator, *ISG15*, as observed in A549 cells.
254
255 Given the presence of PB2 DVGs in cluster 2 of A549 cells, and the association in that cluster
256 between module M100 and the over-expression of ISGs compared to the rest of the cells in the
257 same population as well as to mock-infected cells, we experimentally validated the
258 immunostimulatory impact of PB2 DVGs on the host cells. We infected A549 cells with each of
259 our 3 PR8-DIs (PR8-DI162, -DI222, or -DI244) or with WT virus, and quantified the expression
260 level of ISGs that were shown to be significantly up-regulated in cluster 2 of A549 cells,
261 including *IFI35, IFI27*, and *MX1*, as well as type I and III IFNs that were shown to be significantly
262 up-regulated in cluster 3 of A549 cells (**Supplementary Fig. 17a and 17b**). At 24hpi, we
263 observed a higher induction of the ISGs in DI-infected cells compared to cells infected with WT
264 virus, while a generally higher induction of IFN beta (IFNB) and IFN lambda (IFNL) was
265 observed in the WT-infected cells (**Supplementary Fig. 17c**). Together, these data
266 demonstrated that PB2 DVGs have a strong immunostimulatory effect on the host cells,
267 manifested by a significant induction of ISGs at the late stage of the infection.

DISCUSSION

The goal of this study was to quantitatively and qualitatively characterize viral and host factors that contribute to cell-to-cell transcriptional variation observed during IAV infection. We identified DVGs as potentially important factors in the temporal variation of the host cell transcriptome. The substantial cell-to-cell variation in viral replication and host response that we detected highlight the potential of single-cell virology to provide novel insight into complex virus-host interactions.

The inherent stochasticity of molecular processes, especially during the initial stages of infection, can contribute to the cell-to-cell variation in viral replication [1]. Evidence from studies examining low MOI infections with different virus strains and cell lines suggests that this intrinsic stochasticity can impact viral replication and result in the loss of viral genome segments, transcripts, or proteins [1, 8-10]. Similarly, at different time points of the high MOI infection, we observed cell-to-cell variation in viral transcription, including that in segment-specific transcription. Although the mechanisms leading to this observation are unclear based on our data, it may be explained by the following possibilities as discussed in [10], including (i) the absence of one or more viral genome segments in infecting virions, (ii) a deficiency in intracellular trafficking of incoming viral ribonucleoprotein complexes (vRNPs), (iii) the random degradation of vRNAs prior to transcription, or (iv) mutations resulting in decreased stability of viral mRNAs.

Another source of variability in viral replication stems from the emergence and accumulation of various vRNA species synthesized by the error-prone viral polymerase. Indeed, viral genetic diversity, including amino acid mutations in the NS1 and PB1 proteins, the absence of the NS gene, and an internal deletion in the PB1 gene, contributes to the cell-to-cell variation in the innate immune response as shown in a recent report of low MOI infection [26]. Although the 3’

sequencing strategy employed in our study hinders the identification of mutations in the full-length segments, our experimental setup provides a unique opportunity to evaluate the diversity of DVGs by characterizing the DVG transcripts, since a high MOI infection promotes the accumulation of DVGs. Late stages of infection also emphasize the impact of accumulated DVGs on the host response. We identified a diverse pool of DVG transcripts derived from the 3 polymerase segments, including several dominant species. Notably, the fact that all the dominant DVG PB2 and PB1 transcripts identified in the infected cells were also present in the virus stock, and that the dominant DVG PB1 transcripts were detected in an increasing proportion of cells over the course of infection, suggests potential transmission of DI viruses carrying these DVGs, although the possibility that the regions where the hot spots were located are most prone to polymerase skipping cannot be ruled out.

The accumulation of DVGs can have consequences on viral replication by directly competing with the full-length genomes and modulating host innate immune responses. The immune-modulatory effect of DVGs has been attributed to efficient activation of the IFN induction cascade and antiviral immunity, a mechanism well-known for the non-segmented negative-sense RNA viruses, such as the murine parainfluenza virus Sendai (SeV) (reviewed in [20]). Consistent with previous reports, we detected enrichment of highly expressed genes involved in the IFN response in one subpopulation of cells with significantly attenuated viral transcription; In this cluster of cells we also observed that DVG transcripts accumulated to significantly higher levels. The co-expression network analysis provides us an opportunity to identify modules of co-expressed host genes and directly correlate them with viral factors, such as the level of viral transcription and DVG accumulation, and enables us to identify groups of innate response genes that are potentially differentially expressed under the effect of viral factors. The observation was further validated in our DI- or WT- infection assay, in which we detected a significantly higher expression of some ISGs in DI-infected cells and that of IFNs in WT-infected

cells at the late stage of the infection. Given the fact that some ISGs could be highly expressed in cells with a high level of viral transcription or a high level of DVGs suggests that other viral factors, besides the accumulation of DVGs, may also play an important role in triggering the innate immune response. Nevertheless, unlike SeV DVGs that form “copy-back” structures due to complementary termini generated by “copying back” the authentic 5’ terminus at the 3’ terminus [27, 28], IAV DVGs share identical termini with the full-length genomes. In the copy-back SeV DVGs, a stretch of dsRNA adjacent to a 5’-triphosphate serves as an effective RIG-I ligand [20]; however, the mechanism of IAV DVGs underlying a more effective immunostimulation compared to the full-length genomes remains elusive [20]. A proposed hypothesis is that the unencapsidated replication products of small DVGs can potentially activate RIG-I if they can reach the cytoplasm [20], given the observations *in vitro* and *in vivo* of short influenza RNA template replication in the absence of nucleoprotein (NP) [29]. In addition, the interfering and immune-modulatory abilities of DVGs could also be attributed to DVG-encoded proteins that directly interact with mitochondrial antiviral-signaling (MAVS) and act independently of RIG-I in IFN induction, as previously reported [30].

Our approach enables us to distinguish DVG species accumulated in individual cells and associate the enrichment of certain DVG species with attenuated viral transcription and the induction of innate immune responses with single cell resolution. The accumulation of one type of dominant PB2-DVG (PR8-DI222) in one subpopulation of cells was associated with a strong host innate immune response manifested by over-expression of some ISGs, although the accumulation of other non-dominant defective PB2-DVGs, DVGs derived from other polymerase segments, and certain mutations in stimulating host responses could also have occurred. Considering the significantly attenuated viral transcription in the subpopulation of cells where PR8-DI222 was enriched, the different ability to induce innate immune responses is likely to provide an explanation for the distinct effects of the DVG species. However, further investigation

346 is necessary to pinpoint causal relationships and identify the specific mechanism by which this
347 happens. Our characterization of DVGs and corresponding host responses reveals complex
348 virus-host interactions and an underappreciated single-cell level of immune-modulation by
349 DVGs. The complex gene expression pattern underlying the host innate immune response
350 demonstrates the intricate effects of various viral factors, including—but probably not limited
351 to—the accumulation of DVGs, on shaping infection outcome at the single-cell level.

MATERIALS AND METHODS

Cells and virus

Human lung adenocarcinoma epithelial A549 cells (ATCC, Virginia, USA) were maintained in Kaighn's modified Ham's F-12 medium (F-12K) supplemented with 10% fetal bovine serum (FBS). Primary human bronchial epithelial cells (HBEpC) (PromoCell, Heidelberg, Germany) were maintained in PromoCell airway epithelial cell growth media with SupplementMix (PromoCell). Madin-Darby canine kidney (MDCK) cells were maintained in minimum essential medium (MEM) supplemented with 5% FBS. Human embryonic kidney epithelial 293T cells (ATCC, Virginia, USA) were maintained in Dulbecco's Modified Eagle Medium (DMEM) supplemented with 10% FBS. PB2 protein-expressing modified MDCK (AX4/PB2) [31] cells were maintained in MEM supplemented with 5% Newborn Calf Serum (NBCS), 2 μg/ml puromycin and 1 μg/ml blasticidin. 293T and AX4/PB2 cells were co-cultured with DMEM supplemented with 10% FBS. Viral strain A/Puerto Rico/8/34 (H1N1) was plaque purified and propagated in MDCK cells. Viral titers were determined by plaque assay in MDCK cells and sequences confirmed by Illumina MiSeq sequencing.

Infection assays

Subconfluent monolayers of A549 cells in T-25 flasks were washed with A549 infection media (F-12K supplemented with 0.15% bovine serum albumin (BSA) fraction V and 1% antibiotic-antimycotic) and infected with influenza virus at a multiplicity of infection (MOI) of 5 in 0.5 mL pre-cooled A549 infection media. The flasks were incubated at 4°C for 30 minutes with agitation every 5-10 minutes followed by addition of 4.5 mL pre-warmed A549 infection media and transferred to a 37°C, 5% CO_2 incubator for further incubation. HBEpC cells were infected similarly except the HBEpC infection media was PromoCell airway epithelial cell growth media. The inoculum was back-titrated to confirm the desired MOI was used. The virus-infected cells

were collected at 6, 12, and 24 hours post infection (hpi) and the mock-infected cells were collected at 12 hpi. Cells were extensively washed before re-suspension in PBS containing 0.04% BSA. A proportion of cells from one of the two duplicate flasks per time point were subject to 10X Genomics Chromium single-cell library preparation. The remaining cells in the two flasks were used for conventional bulk RNA-seq library preparation. Notably, due to a failure in the single-cell library preparation for the PR8-infected HBEpC cells collected at 12hpi, we replaced this sample by repeating the same infection assay with HBEpC cells.

Sample preparation, library construction, and sequencing

10X Genomics single cell library preparation with Chromium 3' v2 chemistry was performed following the manufacturer's protocol. A range of 3,900-7,500 cells were used as input into each single cell preparation, with a median of ~3,353 cells (range 2,075-5,254) obtained following sequencing, as described below. Sequencing was performed on the HiSeq 2500 in HighOutput mode (v2) with one library per lane following the manufacturer's recommended sequencing configuration (i.e., paired-end read 1: 27 bp, read 2: 99 bp, and i7 index: 8 bp). An average of 59,200 reads per cell were obtained. For bulk mRNA sequencing, total RNA from two replicate flasks per time point was extracted using RNeasy Mini Kit (Qiagen, Hilden, Germany) with on-column DNA digestion using RNase-free DNase (Qiagen). The conventional bulk RNA-seq library preparation was performed using NEBNext Ultra II RNA library prep kit for Illumina following poly(A) mRNA enrichment. Libraries were multiplexed and sequenced on an Illumina NextSeq 500 in HighOutput 2x75 bp mode (v3). Viral genomic RNA (vRNA) of the virus stocks used in the infection assay was amplified using multi-segment reverse-transcription PCR (M-RTPCR) [32]. The M-RTPCR product was subject to Illumina library preparation with Nextera DNA library prep kit and sequenced on the HiSeq 2500 in Rapid 2x150 bp mode (v2).

Upstream computational analyses of single-cell RNA-seq data

403 The Cell Ranger (v2.1.0) single cell software suite (10X Genomics) was applied to the single-
404 cell RNA-seq data to perform the alignment to the concatenated human (hg19) and influenza A
405 virus (A/Puerto Rico/8/34) reference with STAR (v2.5.3a) [33] and gene counting with the
406 processed UMIs for each cell. The UMI counts for the viral reads with the CIGAR string
407 containing a gap (i.e., "MNM") and different UMI sequences comparing to the ungapped reads
408 were added into the expression matrix later, since they were not considered during gene
409 counting. Given the fact that we performed 3'-end sequencing, transcripts derived from
410 alternative splicing of M and NS segments, encoding M1/M2 and NS1/NEP respectively, could
411 not be distinguished in our analyses, as those transcribed from the same genes share the
412 identical 3'-end.
413
414 To identify and exclude low quality cells in the single cell data from the downstream analyses,
415 the following metrics were calculated for each sample and were employed to filter out cells that
416 failed to meet these criteria: 1) remove cells with fewer than 2,000 detected genes; 2) remove
417 cells with an alignment rate less than the mean minus 3 standard deviations; 3) remove cells
418 with a number of reads after log10 transformation not within 3 standard deviations below or
419 above the mean; 4) remove cells with the number of UMI after log10 transformation not within 3
420 standard deviations below or above the mean; 5) remove cells with the percentage of reads
421 aligned to mitochondrial genes not within 3 standard deviations below or above the mean; 6)
422 remove mock-infected cells with 1 viral read detected. Although we filtered cells based on the
423 size of the total mRNA pool (i.e., total reads) as one of the criteria described above, we also
424 checked the distribution of the size of the host mRNA pool (i.e., host reads) for individual cells.
425 As reported in recent virus-infected single cell studies [9, 34], while virus-induced host shutoff of
426 gene expression [35] is likely to be mainly mediated by host mRNA degradation, it remains
427 unclear what effect viral transcription has on the size of the total mRNA pools. In our study, we
428 observed that virtually all the cells with substantially smaller or larger host mRNA pools–where

the number of host reads after log10 transformation was not within 3 standard deviations below or above the mean–were already being excluded when applying the 6 criteria described above, thus we decided to filter cells based on these. Approximately 120-250 cells were eliminated from each sample, with a median of 164 cells per sample. We further removed genes that were detected in fewer than three cells. After initial cell and gene quality control, the majority of samples had approximately 3,000-3,500 cells left for downstream analysis. The expression levels of host genes were normalized based on the size of the host mRNA pool.

Cell clustering with Seurat

An unsupervised cell clustering to identify subtle changes in the population structure after infection was performed on each time point data separately following the procedures of the Seurat package (v2.1.0) [36] using the normalized, scaled, and centered host gene expression matrix. Briefly, the highly variable genes with average expression < 4 and dispersion > 1 were used as input for the PCA. The statistically significant and biological meaningful PCs determined by the built-in jackstraw and elbow analyses and manually exploration were retained for visualization by t-distributed stochastic neighbor (t-SNE) and subsequent clustering by a shared nearest neighbor (SNN) graph-based approach. The legitimacy of the initially identified clusters was validated using the “ValidateClusters” function in Seurat, which built a support vector machine (SVM) classifier with significant PCs and then applied the accuracy cutoffs of 0.9 and the minimal connectivity threshold of 0.001. To identify markers that are differentially expressed among clusters, the “FindMarkers” function in Seurat was used with the different test options, including “bimod” [37], “poisson”, “negbinom”, and “MAST” (v1.4.1) [38]. Only the genes that showed at least 0.25-fold difference on the log-scale between two groups and were expressed in at least 25% of the cells in either group were tested for differential expression. Significantly differentially expressed genes for each cluster (i.e., the markers) were identified by applying the adjusted p-value cut-off of 0.05. Markers identified by all four methods were retained. GO term

455 over-representation analysis of the up-regulated markers was performed with the online service
456 DAVID [39, 40] by applying the Benjamini p-value cut-off of 0.05. To determine the cell cycle
457 stage associated with individual cells, cell-cycle scoring and assignment were performed with
458 Seurat using the “CellCycleScoring” function based on the expression of canonical markers [41].
459
460 **Computational analyses of bulk RNA-seq and virus stock sequencing data**
461 The raw bulk RNA-seq and virus stock sequencing data was first trimmed with trimmomatic
462 (v0.36) [42] to remove the adaptors and trim off low quality bases. Reads with a minimal length
463 of 36 bases in the trimmed bulk RNA-seq dataset were aligned to the concatenated human
464 (hg19) and influenza A/Puerto Rico/8/34 (H1N1) reference with STAR (v2.5.3a) [33] with the
465 default parameters, and counted with featureCounts [43] in the Subread package (v1.5.1) [44],
466 while reads in the virus stock sequencing dataset were aligned to the influenza A/Puerto
467 Rico/8/34 (H1N1) reference with STAR (v2.5.3a) [33]. Differential expression analysis was
468 performed with DESeq2 (v1.18.1) [45] and edgeR (v3.20.5) [46, 47] using the bulk RNA-seq and
469 the merged single-cell RNA-seq data. Host genes with the adjusted p-value < 0.05 were
470 identified as significantly differentially expressed at each time point.
471
472 **Deletion junction identification, filtering, and quantification**
473 Reads that aligned to both ends of the polymerase segments, and that contained large internal
474 deletions (i.e. ≥ 1000 nucleotides, with each aligned portion of at least 10 nucleotides in length)
475 were collected. Following UMI de-duplication, reads with junction coordinates within a 10-
476 nucleotide window were grouped together. We excluded from downstream analyses reads with
477 junction coordinates that occurred fewer than 10 times in each sample. To compare
478 quantitatively gap-spanning reads for each segment across cells and samples, the number of
479 gap-spanning reads was normalized to the total number of non-gap-spanning reads aligned to a
480 100nt region centering the coverage peak at the 3’ end. As cells with low infection (especially

481 those harvested at the early stage of infection or inoculated at a low MOI) typically have poor
482 coverage for the viral segments of interest, the DVG/FL ratio in those cells calculated as
483 described above is typically inflated and may even fail to be calculated because all the viral
484 reads corresponding to a given segment are gap-spanning or there are no viral reads. To
485 mitigate this effect, we overwrote those values to 0 in the datasets, including the dataset
486 collected from HBEpC cells at 6hpi.
487
488 **Generation of PR8-derived DI162 and DI222 virus**
489 To generate the PR8 PB2-DI162, -DI222, and -DI244 reverse genetics plasmids, gBlocks Gene
490 Fragments (Integrated DNA Technologies, California, USA) were ordered using the
491 corresponding defective PB2 genomic sequences identified in this study (PR8-DI162 and PR8-
492 DI222) or previously reported (DI244) [18] and cloned into the pBZ61A18 reverse genetics
493 vector as previously described [48]. To rescue the PR8 DI viruses, each of the sequence
494 confirmed PB2-DI plasmids was co-transfected into 293T-AX4/PB2 co-cultured cells with the 7
495 reverse genetics plasmids for PR8 PB1, PA, HA, NP, NA, M, and NS and a PB2 protein-
496 expression plasmid using Lipofectamine™ 3000 Transfection Reagent (Invitrogen, California,
497 USA). The supernatant was collected on day 2 post-infection and passaged twice in the
498 AX4/PB2 cell line, which expresses the PB2 protein in *trans* [31]. Viral titers were determined by
499 TCID50 assay in AX4/PB2 cells.
500
501 **Interference test for PR8-DI162 and PR8-DI222 viruses and validation of their**
502 **immunostimulatory effects**
503 To test the interfering ability of PR8-DI162 and PR8-DI222 viruses that carry the deletions
504 identified in two dominant PB2-DVG species from the single cell dataset, their inhibitory effects
505 on wild type PR8 virus replication was quantified in cultured cells. Subconfluent monolayers of
506 A549 cells in 12-well plates were washed with infection media (MEM supplemented with 0.15%

BSA fraction V, 1% antibiotic-antimycotic and 1 μg/mL TPCK-treated trypsin) and each well was co-infected with one type of DI virus at a MOI of 5 and the PR8 virus at a MOI of 0.005 in 1 mL infection media. Plates were transferred to a 37°C, 5% CO_2 incubator. At 2 hours post infection, and 1, 2, and 3 days post infection, supernatants were collected and wild type PR8 yield was determined by TCID50 assay using MDCK cells, which do not support replication of DI viruses due to the lack of functional PB2 proteins.

To determine if the DI viruses could stimulate a higher expression of some ISGs identified in the network analysis, subconfluent monolayers of A549 cells in 12-well plates were infected with each DI virus (PR8-DI162, -DI222, or -DI244) or WT virus at a MOI of 10 in triplicate. Total RNA from cells collected at 24hpi was extracted using RNeasy Mini Kit (Qiagen, Hilden, Germany). 100ng RNA was subsequently used as template for reverse transcription using SuperScript IV system (Invitrogen, California, USA) with Oligo $d(T)_{20}$ primer. qPCR was performed using PowerUp SYBR Green (Applied Biosystems, Massachusetts, USA) in triplicate with the following primers: IFI35: Hs.PT.58.38490206 (IDT, Iowa, USA); IFI27: IFI27fw (5'-GCCTCTGGCTCTGCCGTAGTT-3') and IFI27rev (5'-ATGGAGGACGAGGCGATTCC-3') [49]; MX1: MX1fw (5'-CTTTCCAGTCCAGCTCGGCA-3') and MX1rev (5'-AGCTGCTGGCCGTACGTCTG-3') [49]; IFNB: IFNBfw (5'-TCTGGCACAACAGGTAGTAGGC-3') and IFNBrev (5'-GAGAAGCACAACAGGAGAGCAA-3') [50]; IFNL: IFNLfw (5'-GCCCCCAAAAAGGAGTCCG-3') and IFNLrev (5'-AGGTTCCCATCGGCCACATA-3') [50]; β-actin (ACTB): ACTBfw (5'-GAACGGTGAAGGTGACAG-3') and ACTBrev (5'-TTTAGGATGGCAAGGGACT-3') [51]. For all the targets, qPCR parameters according to manufacturer's recommendation were: 95°C for 10 min and then 45 cycles of 95°C for 15 s, 57°C for 15 s, and 60°C for 60 s. Fold change of target gene expression was calculated using the $2^{-\Delta\Delta C_T}$ method normalized to ACTB.

532

533 **Gene co-expression network analysis**

534 Multiscale Embedded Gene Co-Expression Network Analysis (MEGENA) [25] was performed to
535 identify host modules of highly co-expressed genes in influenza infection. The MEGENA
536 workflow comprises 4 major steps: 1) Fast Planar Filtered Network construction (FPFNC), 2)
537 Multiscale Clustering Analysis (MCA), 3) Multiscale Hub Analysis (MHA), 4) and Cluster-Trait
538 Association Analysis (CTA). A cutoff of 0.05 after perturbation-based FDR calculation was used.
539 The total relevance of each module to influenza infection was calculated by summarizing the
540 combined enrichment of the differentially expressed disease gene (DEDG) signatures: $G_j = \prod_i g_{ji}$,
541 where, g_{ji} is the relevance of a module ***j*** to a signature ***i;*** and g_{ji} is defined as
542 $(max_j(r_{ji}) + 1 - r_{ji})/\sum_j r_{ji}$, where r_{ji} is the ranking order of the significance level of the overlap
543 between the module ***j*** and the signature ***i***. Here, DEDGs are differently expressed genes
544 between virus-infected cells of a particular cluster and the bulk of mock-infected cells
545 determined by t-test. Only the genes that showed at least 0.25-fold difference on the log-scale
546 between two groups and were expressed in at least 25% of the cells in either group were tested
547 for differential expression. Significantly differentially expressed genes were identified by
548 applying the adjusted p-value cut-off of 0.05.

549

550 **Identification of enriched pathways, key regulators in the host module, relative**
551 **abundance of virus transcripts as well as DVGs associated with host modules**

552 To functionally annotate gene signatures and gene modules identified in this study, enrichment
553 analysis was performed of the established pathways and signatures—including the gene
554 ontology (GO) categories and MSigDB—and the subject area-specific gene sets—including
555 influenza host factors, Inflammasome, Interferome, and InnateDB. The hub genes in each
556 subnetwork were identified using the adopted Fisher's inverse Chi-square approach in

MEGENA; Bonferroni-corrected p-values smaller than 0.05 were set as the threshold to identify significant hubs.

The relative abundance of virus transcripts and the DVGs associated with the host modules were identified using Spearman correlation between the first principal component of the gene expression in the corresponding module and the traits, including the relative abundance of each or total viral transcripts and the DVG/FL ratio. Significantly associated traits were identified using the Benjamini-Hochberg FDR-corrected p-value 0.05 as the cutoff.

STATISTICAL ANALYSIS

The statistical significance of the changes in the relative abundance of viral and DVG transcripts between 3 or more groups of cells was first determined by the one- or two- tailed Kruskal-Wallis rank sum test, followed by the one-tailed Wilcoxon rank sum test to calculate the pairwise comparisons. The statistical significance of expression fold changes in the qPCR validation assay was determined using the two-tailed Student's *t*-test. A p-value of ≤ 0.05 was considered statistically significant.

CODE AVAILABILITY

The code used to generate all the results is available on Github (https://github.com/GhedinLab/Single-Cell-IAV-infection-in-monolayer).

DATA AVAILABILITY

Sequencing data that support the findings of this study have been deposited in the Gene Expression Omnibus (GEO) repository with the accession codes GSE118773 (currently private record).

583 **ACKNOWLEDGEMENTS**

584 We thank members of the Ghedin laboratory for feedback and discussion. We thank Tara Rock,
585 Nicholas Rouilard, Olivia Micci-Smith, and Mohammed Khalfan of the Genomics Core Facility at
586 the Center for Genomics and Systems Biology, New York University for sequencing. We thank
587 Yoshihiro Kawaoka for providing the AX4/PB2 cells and Peter Palese and Adolfo Garcia-Sastre
588 for providing the PR8 RGs plasmids. This work was supported by NIAID/NIH U01 AI111598.
589 This work was also supported in part through the NYU IT High Performance Computing
590 resources, services, and staff expertise.

591

592 **AUTHOR CONTRIBUTIONS**

593 All authors read and approved the manuscript. E.G. conceived and designed the experiments,
594 supervised research, and wrote the manuscript. B. Zhou conceived and designed the
595 experiments, supervised research, performed the infection assays, and wrote the manuscript**.**
596 C.W. performed the infection assays and bulk RNA-seq library preparation, analyzed the data,
597 and wrote the manuscript. C.V.F. performed the network analysis and wrote the manuscript. T.C.
598 performed the DI virus generation, interfering, and validation assay and wrote the manuscript.
599 A.G. performed the library preparation for the virus stock. M.W. and B. Zhang contributed to
600 data analyses. W.H., M.S., and R.S. performed the single-cell library preparation.

601

602

REFERENCES

1. Heldt FS, Kupke SY, Dorl S, Reichl U, Frensing T. Single-cell analysis and stochastic modelling unveil large cell-to-cell variability in influenza A virus infection. Nature Communications. 2015;6:8938.
2. Guo F, Li S, Caglar MU, Mao Z, Liu W, Woodman A, et al. Single-cell virology: On-chip investigation of viral infection dynamics. Cell Reports. 2017;21(6):1692-704.
3. Raj A, van Oudenaarden A. Nature, nurture, or chance: Stochastic gene expression and its consequences. Cell. 2008;135(2):216-26.
4. Lwoff A, Dulbecco R, Vogt M, Lwoff M. Kinetics of the release of poliomyelitis virus from single cells. Virology. 1955;1(1):128-39.
5. Zhu Y, Yongky A, Yin J. Growth of an RNA virus in single cells reveals a broad fitness distribution. Virology. 2009;385(1):39-46.
6. Timm A, Yin J. Kinetics of virus production from single cells. Virology. 2012;424(1):11-7.
7. Zanini F, Pu S-Y, Bekerman E, Einav S, Quake SR. Single-cell transcriptional dynamics of flavivirus infection. eLife. 2018;7:e32942.
8. Dou D, Hernandez-Neuta I, Wang H, Ostbye H, Qian X, Thiele S, et al. Analysis of IAV replication and co-infection dynamics by a versatile RNA viral genome labeling method. Cell Reports. 2017;20(1):251-63.
9. Russell AB, Trapnell C, Bloom JD. Extreme heterogeneity of influenza virus infection in single cells. eLife. 2018;7:e32303.
10. Brooke CB, Ince WL, Wrammert J, Ahmed R, Wilson PC, Bennink JR, et al. Most influenza a virions fail to express at least one essential viral protein. Journal of Virology. 2013;87(6):3155-62.
11. Henle W, Henle G. Interference of inactive virus with the propagation of virus of influenza A. Science. 1943;98(2534):87-9.
12. von Magnus P. Incomplete Forms of Influenza Virus. Advances in Virus Research Volume 2. Advances in Virus Research1954. p. 59-79.
13. Davis AR, Nayak DP. Sequence relationships among defective interfering influenza viral RNAs. Proceedings of the National Academy of Sciences of the United States of America. 1979;76(7):3092-6.
14. Nayak DP, Chambers TM, Akkina RK. Defective-Interfering (DI) RNAs of Influenza Viruses: Origin, Structure, Expression, and Interference. Current Topics in Microbiology and Immunology. 114. 1st ed. Berlin Heidelberg: Springer-Verlag; 1985. p. 103-51.
15. Saira K, Lin X, DePasse JV, Halpin R, Twaddle A, Stockwell T, et al. Sequence analysis of in vivo defective interfering-like RNA of influenza A H1N1 pandemic virus. Journal of Virology. 2013;87(14):8064-74.
16. Vasilijevic J, Zamarreno N, Oliveros JC, Rodriguez-Frandsen A, Gomez G, Rodriguez G, et al. Reduced accumulation of defective viral genomes contributes to severe outcome in influenza virus infected patients. PLos Pathogens. 2017;13(10):e1006650.
17. Dimmock NJ, Easton AJ. Defective interfering influenza virus RNAs: time to reevaluate their clinical potential as broad-spectrum antivirals? Journal of Virology. 2014;88(10):5217-27.
18. Dimmock NJ, Rainsford EW, Scott PD, Marriott AC. Influenza virus protecting RNA: an effective prophylactic and therapeutic antiviral. Journal of Virology. 2008;82(17):8570-8.
19. Baum A, Sachidanandam R, García-Sastre A. Preference of RIG-I for short viral RNA molecules in infected cells revealed by next-generation sequencing. PNAS. 2010;107(37):16303-8.
20. Killip MJ, Fodor E, Randall RE. Influenza virus activation of the interferon system. Virus Research. 2015;209:11-22.
21. Janda MJ, Davis AR, Nayak DP, De BK. Diversity and generation of defective interfering influenza virus particles. Virology. 1979;95(1):48-58.

22. Chen S, Short JA, Young DF, Killip MJ, Schneider M, Goodbourn S, et al. Heterocellular induction of interferon by negative-sense RNA viruses. Virology. 2010;407(2):247-55.
23. He Y, Xu K, Keiner B, Zhou J, Czudai V, Li T, et al. Influenza A virus replication induces cell cycle arrest in G0/G1 phase. Journal of Virology. 2010;84(24):12832-40.
24. Jiang W, Wang Q, Chen S, Gao s, Song L, Liu P, et al. Influenza A virus NS1 induces G0/G1 cell cycle arrest by inhibiting the expression and activity of RhoA protein. Journal of Virology. 2013;87(6):3039-52.
25. Song W-m, Zhang B. Multiscale embedded gene co-expression network analysis. PLOS Computational Biology. 2015;11(11):e1004574.
26. Russell AB, Kowalsky JR, Bloom JD. Single-cell virus sequencing of influenza infections that trigger innate immunity; 2018. Preprint. Available from: bioRxiv: https://doi.org/10.1101/437277. Cited Oct 7, 2018.
27. Re GG, Gupta KC, Kingsbury DW. Genomic and copy-back 3' termini in Sendai virus defective interfering RNA species. Journal of Virology. 1983;45(2):659-64.
28. Strahle L, Garcin D, Kolakofsky D. Sendai virus defective-interfering genomes and the activation of interferon-beta. Virology. 2006;351(1):101-11.
29. Turrell L, Lyall JW, Tiley LS, Fodor E, Vreede FT. The role and assembly mechanism of nucleoprotein in influenza A virus ribonucleoprotein complexes. Nature Communications. 2013;4:1591.
30. Boergeling Y, Rozhdestvensky TS, Schmolke M, Resa-Infante P, Robeck T, Randau G, et al. Evidence for a novel mechanism of influenza virus-induced type I interferon expression by a defective RNA-encoded protein. PLoS Pathogens. 2015;11(5):e1004924.
31. Ozawa M, Victor ST, Taft AS, Yamada S, Li C, Hatta M, et al. Replication-incompetent influenza A viruses that stably express a foreign gene. Journal of General Virology. 2011;92:2879-88.
32. Zhou B, Donnelly ME, Scholes DT, George KS, Hatta M, Kawaoka Y, et al. Single-reaction genomic amplification accelerates sequencing and vaccine production for classical and swine origin human influenza A viruses. Journal of Virology. 2009;83(19):10309-13.
33. Dobin A, Davis CA, Schlesinger F, Drenkow J, Zaleski C, Jha S, et al. STAR: ultrafast universal RNA-seq aligner. Bioinformatics. 2013;29(1):15-21.
34. Steuerman Y, Cohen M, Peshes-Yaloz N, Valadarsky L, Cohn O, David E, et al. Dissection of influenza infection in vivo by single-cell RNA sequencing. Cell Systems. 2018;6(6):679-91 e4.
35. Bercovich-Kinori A, Tai J, Gelbart IA, Shitrit A, Ben-Moshe S, Drori Y, et al. A systematic view on influenza induced host shutoff. eLife. 2016;5:e18311.
36. Satija R, Farrell JA, Gennert D, Schier AF, Regev A. Spatial reconstruction of single-cell gene expression data. Nature Biotechnology. 2015;33(5):495-502.
37. McDavid A, Finak G, Chattopadyay PK, Dominguez M, Lamoreaux L, Ma SS, et al. Data exploration, quality control and testing in single-cell qPCR-based gene expression experiments. Bioinformatics. 2013;29(4):461-7.
38. Finak G, McDavid A, Yajima M, Deng J, Gersuk V, Shalek AK, et al. MAST: a flexible statistical framework for assessing transcriptional changes and characterizing heterogeneity in single-cell RNA sequencing data. Genome Biology. 2015;16:278.
39. Huang DW, Sherman BT, Lempicki RA. Systematic and integrative analysis of large gene lists using DAVID Bioinformatics Resources. Nature Protocol. 2009;4(1):44-57.
40. Huang DW, Sherman BT, Lempicki RA. Bioinformatics enrichment tools: paths toward the comprehensive functional analysis of large gene lists. Nucleic Acids Research. 2009;37(1):1-13.
41. Kowalczyk MS, Tirosh I, Heckl D, Rao TN, Dixit A, Haas BJ, et al. Single-cell RNA-seq reveals changes in cell cycle and differentiation programs upon aging of hematopoietic stem cells. Genome Research. 2015;25(12):1860-72.

42. Bolger A, Lohse M, Usadel B. Trimmomatic: a flexible trimmer for Illumina sequence data. Bioinformatics. 2014;30(15):2114-20.
43. Liao Y, Smyth G, Shi W. featureCounts: an efficient general purpose program for assigning sequence reads to genomic features. Bioinformatics. 2014;30(7):923-30.
44. Liao Y, Smyth G, Shi W. The Subread aligner: fast, accurate and scalable read mapping by seed-and-vote. Nucleic Acids Research. 2013;41(10):e108.
45. Love M, Huber W, Anders S. Moderated estimation of fold change and dispersion for RNA-seq data with DESeq2. Genome Biology. 2014;15:550.
46. Robinson M, McCarthy D, Smyth G. edgeR: a Bioconductor package for differential expression analysis of digital gene expression data. Bioinformatics. 2010;26(1):139-40.
47. McCarthy D, Chen Y, Smyth G. Differential expression analysis of multifactor RNA-seq experiments with respect to biological variation. Nucleic Acids Research. 2012;40(10):4288-97.
48. Zhou B, Wentworth DE. Influenza A Virus Molecular Virology Techniques. In: Kawaoka Y, Neumann G, editors. Influenza Virus Methods in Molecular Biology (Methods and Protocols). 865: Humana Press; 2012.
49. Cheon H, Holvey-Bates EG, Schoggins JW, Forster S, Hertzog P, Imanaka N, et al. IFNβ-dependent increases in STAT1, STAT2, and IRF9 mediate resistance to viruses and DNA damage. EMBO Journal. 2013;32(30):2751-63.
50. Zhou B, Li Y, Belser JA, Pearce MB, Schmolke M, Subba AX, et al. NS-based live attenuated H1N1 pandemic vaccines protect mice and ferrets. Vaccine. 2010;28(50):8015-25.
51. Mayanagi T, Morita T, Hayashi K, Fukumoto K, Sobue K. Glucocorticoid receptor-mediated expression of caldesmon regulates cell migration via the reorganization of the actin cytoskeleton. Journal of Biological Chemistry. 2008;283(45):31183-96.

729 **FIGURES**

Fig 1.

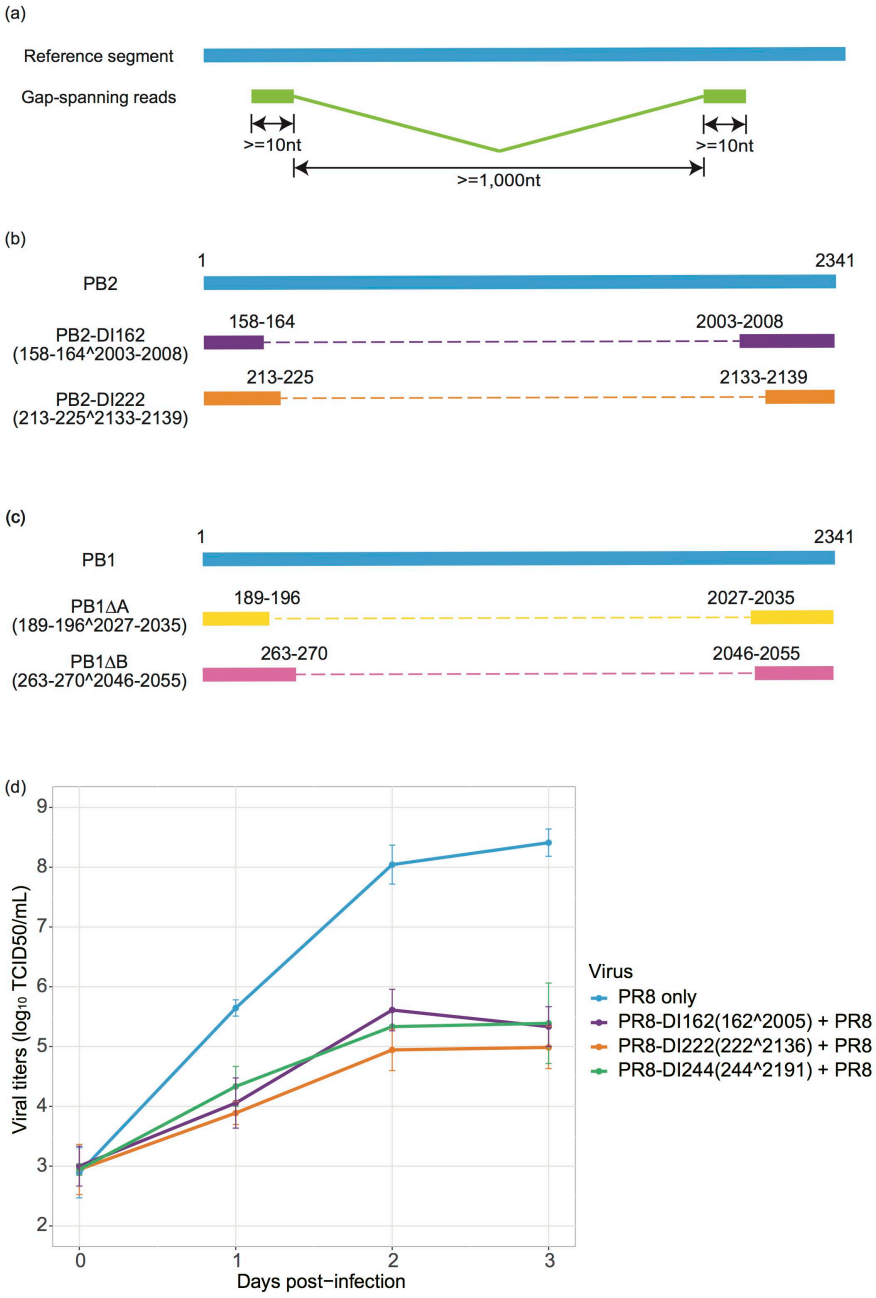

730

731 **Figure 1. Characterization of DVG transcripts and validation of interfering capacity. (a)**
732 Selection criteria for reads considered to be representatives of DVGs. Given the length of the
733 reads, we required that each portion of the gap-spanning reads were at least 10 bp in length.
734 Considering that DVGs typically lose approximately 80% of their original sequences, we also

735 required that the size of the gap should be at least 1 kb. **(b-c)** Schematic diagram showing two
736 types of defective viral transcripts derived from **(b)** PB2 and **(c)** PB1 segments, respectively.
737 The caret "^" denotes a deletion event and the numbers before and following it indicate the
738 coordinates of the junction sites. **(d)** Interfering capacity of generated defective interfering
739 particles (DIs) carrying identified deletion sites in the PB2 segment during co-infection with the
740 WT-PR8 virus. A549 cells were co-infected with WT virus and one type of DI virus at a ratio of
741 1:1000. Viral titers at 2 hours post-infection (denoted as day 0 post-infection) and 1 to 3 days
742 post-infection (dpi) were measured by the TCID50 assay on MDCK cells. Three types of DI
743 viruses were tested, including two DI viruses identified in this study and a previously reported
744 DI244 virus [18] that has been considered as a potential candidate for antiviral therapy [17]. For
745 each type of DI virus, the information about the junction sites was denoted in parentheses. The
746 error bar representing the standard deviation of the mean was obtained from three biological
747 replicates.
748

Fig 2.

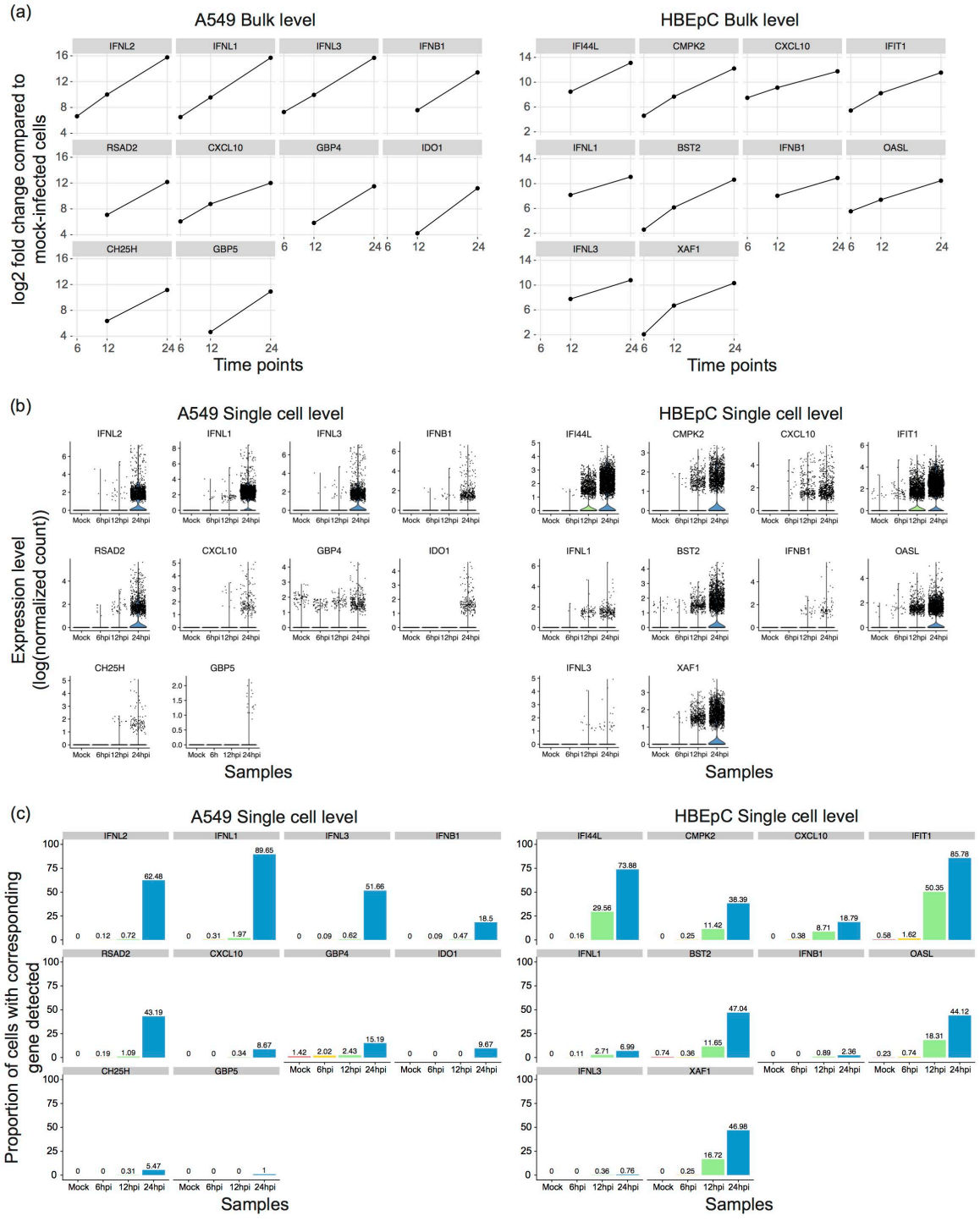

Figure 2. Comparison of the induction of interferons (IFNs) and interferon-stimulated genes (ISGs) at bulk and single-cell levels. (a) Log2 fold changes of the top 10 differentially expressed genes with the greatest fold change by 24hpi, including type I and III IFNs and some

753 ISGs, compared to mock-infected cells detected in A549 and HBEpC cells over the course of
754 the infection at the bulk level. The results from edgeR are shown. **(b)** The expression of these
755 genes at the single-cell level over the course of the infection in two cell types. Expression was
756 calculated as log-transformed UMI counts normalized by the host library size. The violins below
757 the dots are colored by samples. **(c)** Proportion of cells in which these genes are detected over
758 the course of the infection in two cell types. The colors are consistent with those in panel (b).

Fig 3.

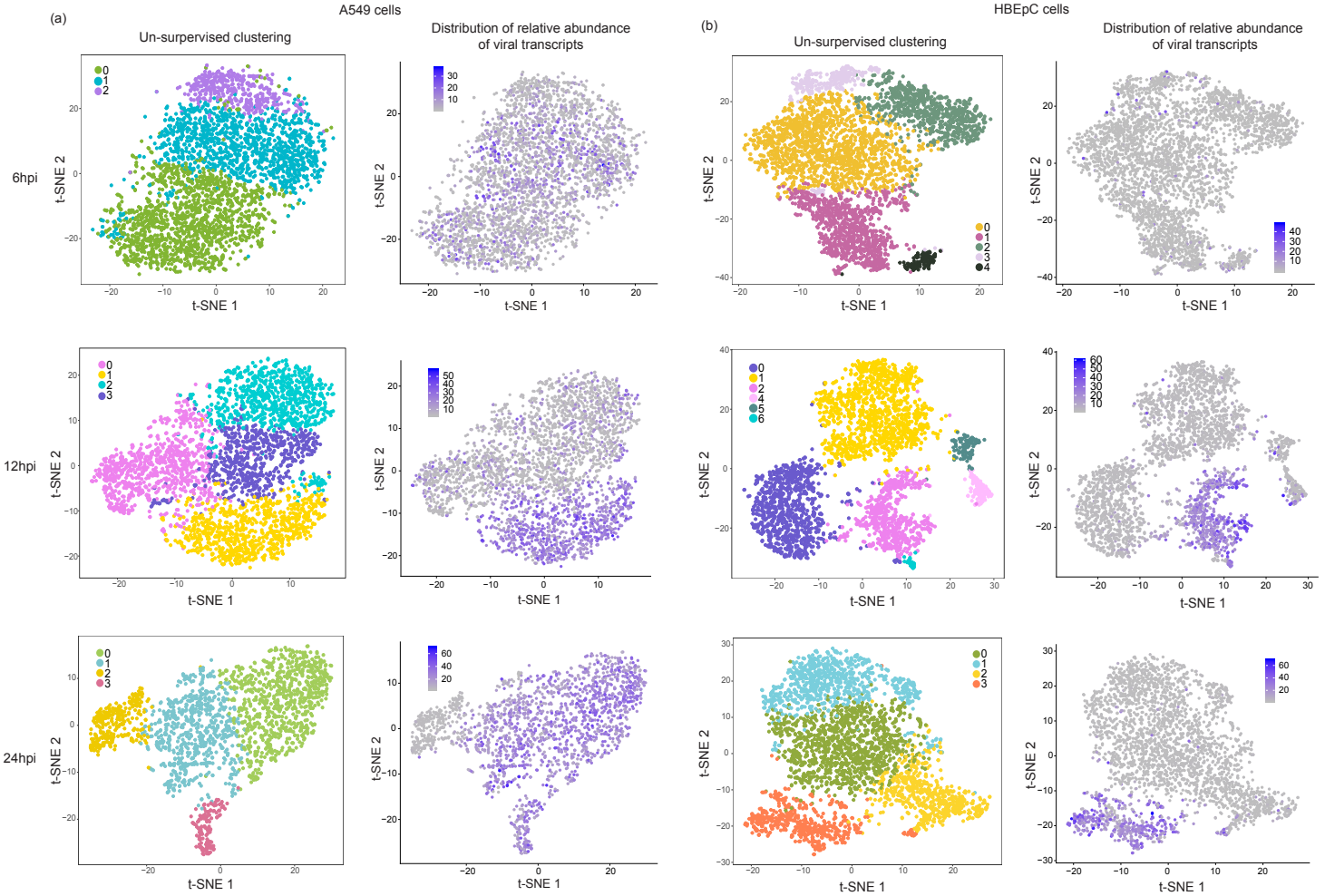

759

760 **Figure 3. Comparison of cell clustering patterns and the distribution of viral transcript relative abundance.** PR8-infected **(a)**

761 A549 and **(b)** HBEpC cells harvested at each time point were subjected to un-supervised clustering based on the host transcriptome

and visualized on a t-SNE plot. Each dot on a t-SNE plot represents a cell. Cell clustering patterns, in which cells were colored by their cluster identity, are shown in the left panels, and the distribution of the relative abundance of viral transcripts at different time points in individual cells is shown in the right panels.

Fig 4.

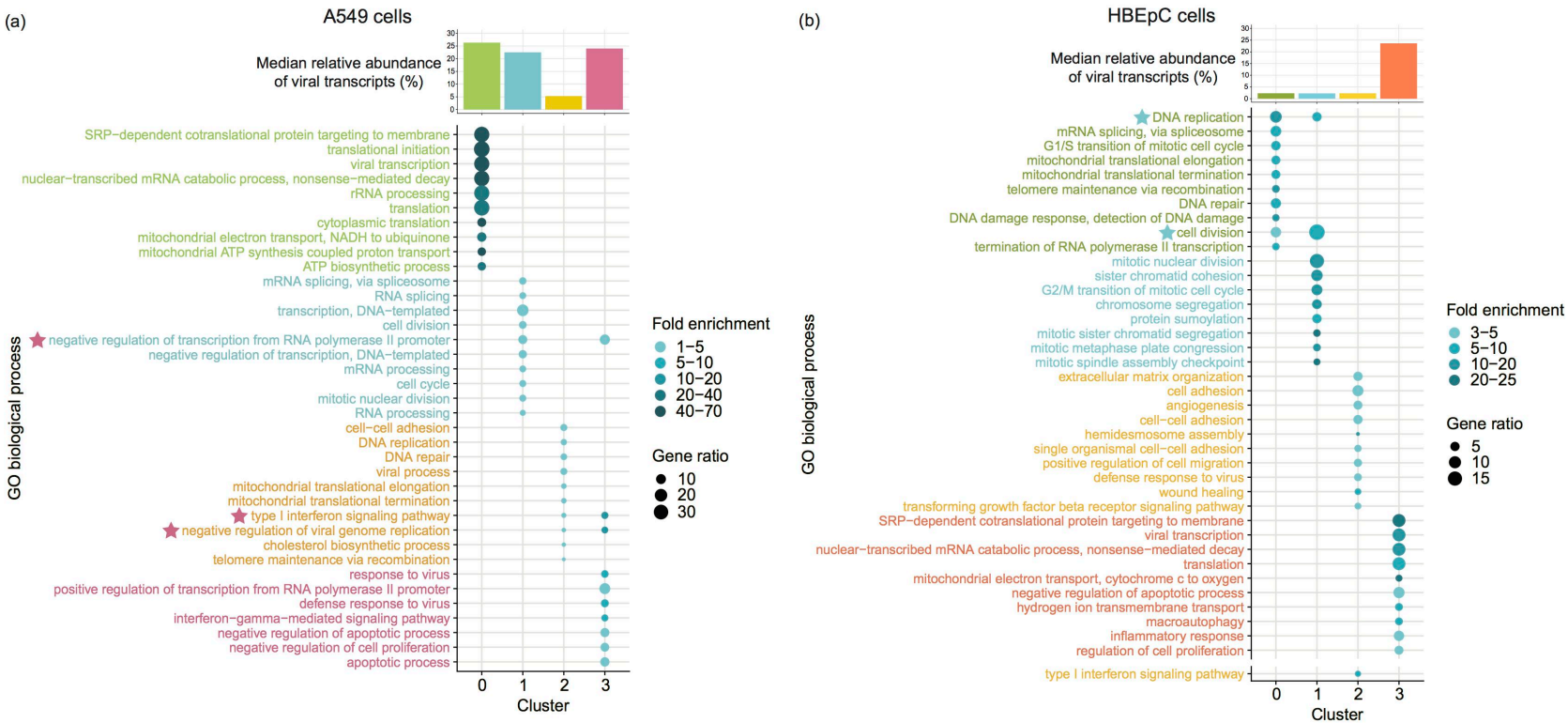

Figure 4. Enriched biological process gene ontology (GO) terms in A549 cells at 24hpi. (a-b) Biological process GO terms associated with over-expressed genes in each cluster of (**a**) A549 and (**b**) HBEpC cells. The top 10 over-represented GO terms in each cluster are shown in the upper panel and another over-represented GO term related to type I IFN signaling pathway in clusters 2 of HBEpC cells are shown in the lower panel. Redundant GO terms in HBEpC cells were collapsed. Each GO term is denoted by a dot. The color intensity of each dot indicates the fold enrichment of the corresponding GO term and the size corresponds to the ratio of queried genes in the gene set associated with a given GO term. The GO terms enriched in each cluster are color-coded by

clusters. The asterisks in the upper panel denote the GO terms enriched in two clusters and their colors indicate the identity of the other cluster besides the one denoted by the color of the GO term. The bar chart above the bubble chart of the GO terms shows the median relative abundance of the viral transcripts across cells in each cluster. The colors of the bar are consistent with that of the GO terms.

Fig 5.

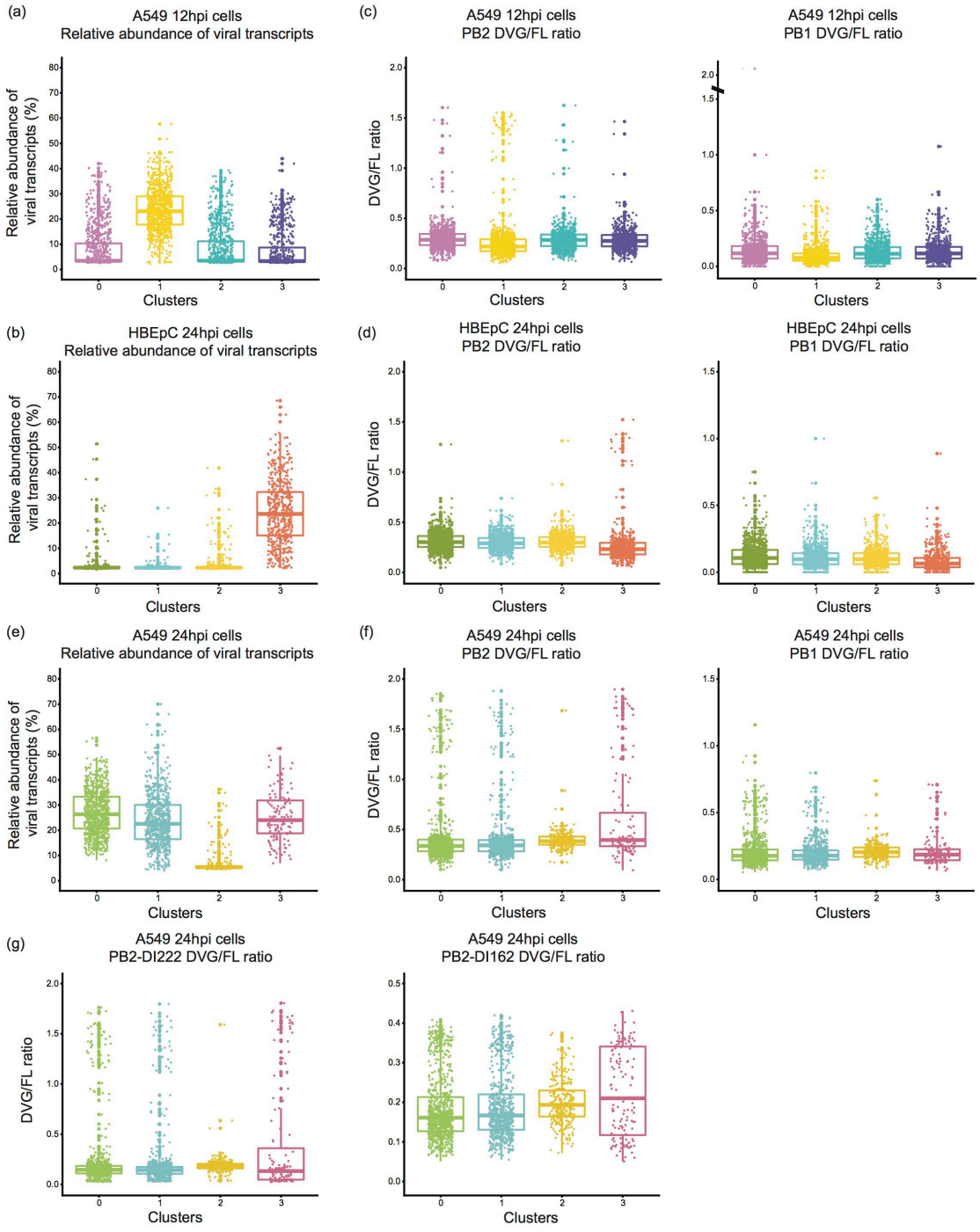

Figure 5. Distribution of the relative abundance of viral transcripts and DVG/FL ratio for DVG PB2 and PB1 transcripts in each cluster of cells. (a, b, and e) Box-plot of the relative abundance of viral transcripts in each cluster of **(a)** A549 cells at 12hpi, **(e)** 24hpi, and **(b)** HBEpC cells at 24hpi. **(c, d, and f)** The DVG/FL ratio for DVG PB2 and PB1 transcripts

781 calculated as the ratio of gap-spanning reads to non-gap-spanning reads aligned to a 3'
782 coverage peak region derived from the corresponding viral segments in each cluster. **(g)** The
783 DVG/FL ratio for DVG PB2 transcripts carrying deletion sites similar to those in PR8-DI222 and
784 PR8-DI162 viruses in each cluster of A549 cells at 24hpi. All box plots show the first and third
785 quantiles as the lower and upper hinges, the median in the center, and 1.5 * inter-quartile range
786 (IQR) from the first and third quantiles as the whiskers.
787

Fig 6.

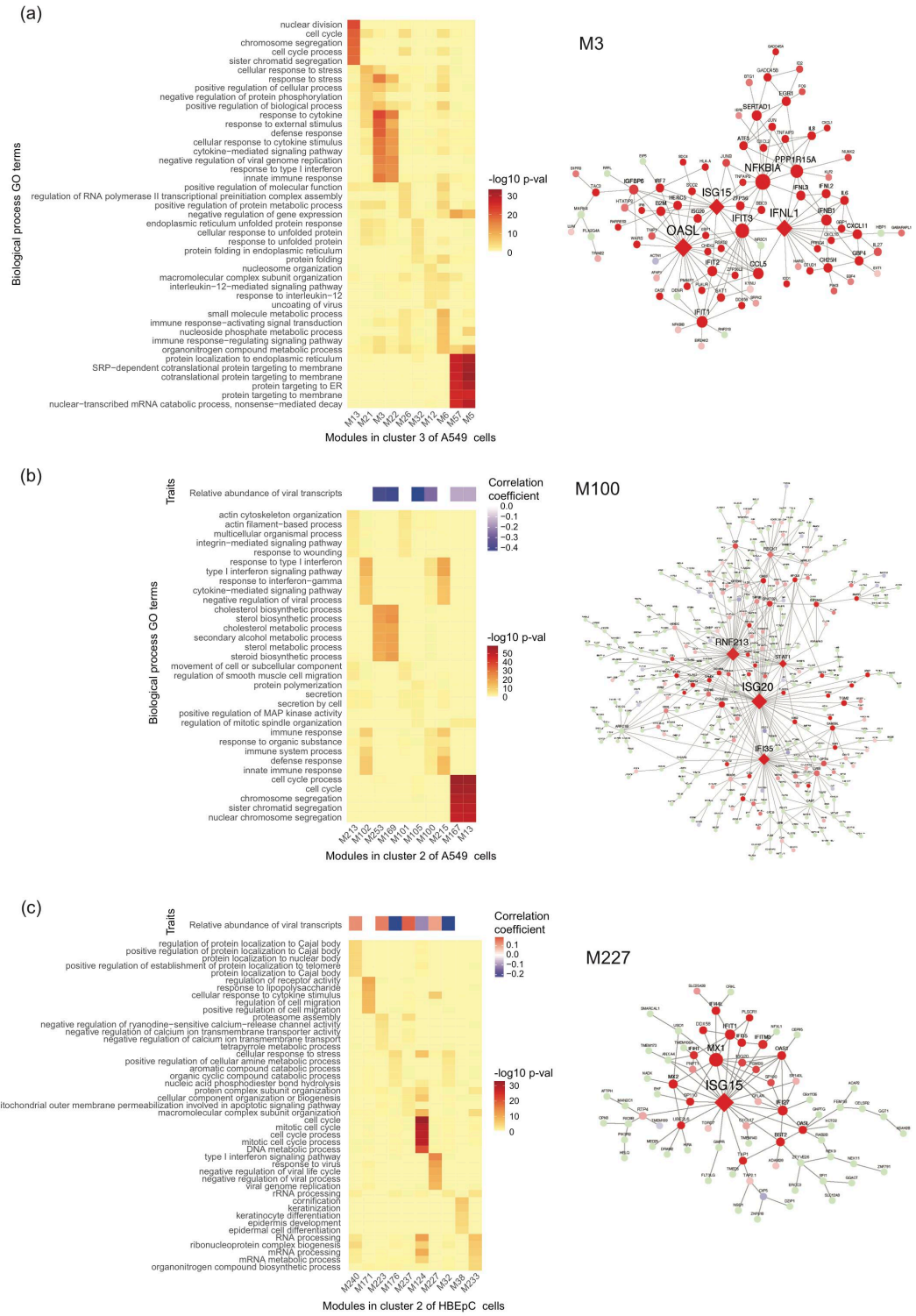

Figure 6. Functional MEGENA modules in clusters of A549 and HBEpC cells at 24hpi. Left panels show heatmaps of enriched biological process GO terms in the top 10 best ranked

791 modules in clusters **(a)** 3 and **(b)** 2 of A549 cells as well as **(c)** cluster 2 of HBEpC cells at 24hpi
792 and the correlation between modules and the level of viral transcription. Colors in the heatmaps
793 of GO terms indicate FET p-values after GO enrichment. Red and blue colors in the correlation
794 heatmaps denote positive or negative correlation with corresponding modules, respectively.
795 Right panels show the MEGENA network of modules enriched with innate immune response,
796 including **(a)** module M3 in cluster 3 of A549 cells, **(b)** module M100 in cluster 2 of A549 cells, **(c)**
797 module M227 in cluster 2 of HBEpC cells. Red and blue nodes represent significantly up- or
798 down-regulated genes compared to all mock-infected cells, while light-green nodes denote
799 genes that are not significantly differentially expressed. Diamond nodes indicate key regulators.
800 The size of the nodes indicates node strength after Multiscale Hub Analysis within the MEGENA
801 pipeline.
802

SUPPORTING INFORMATION

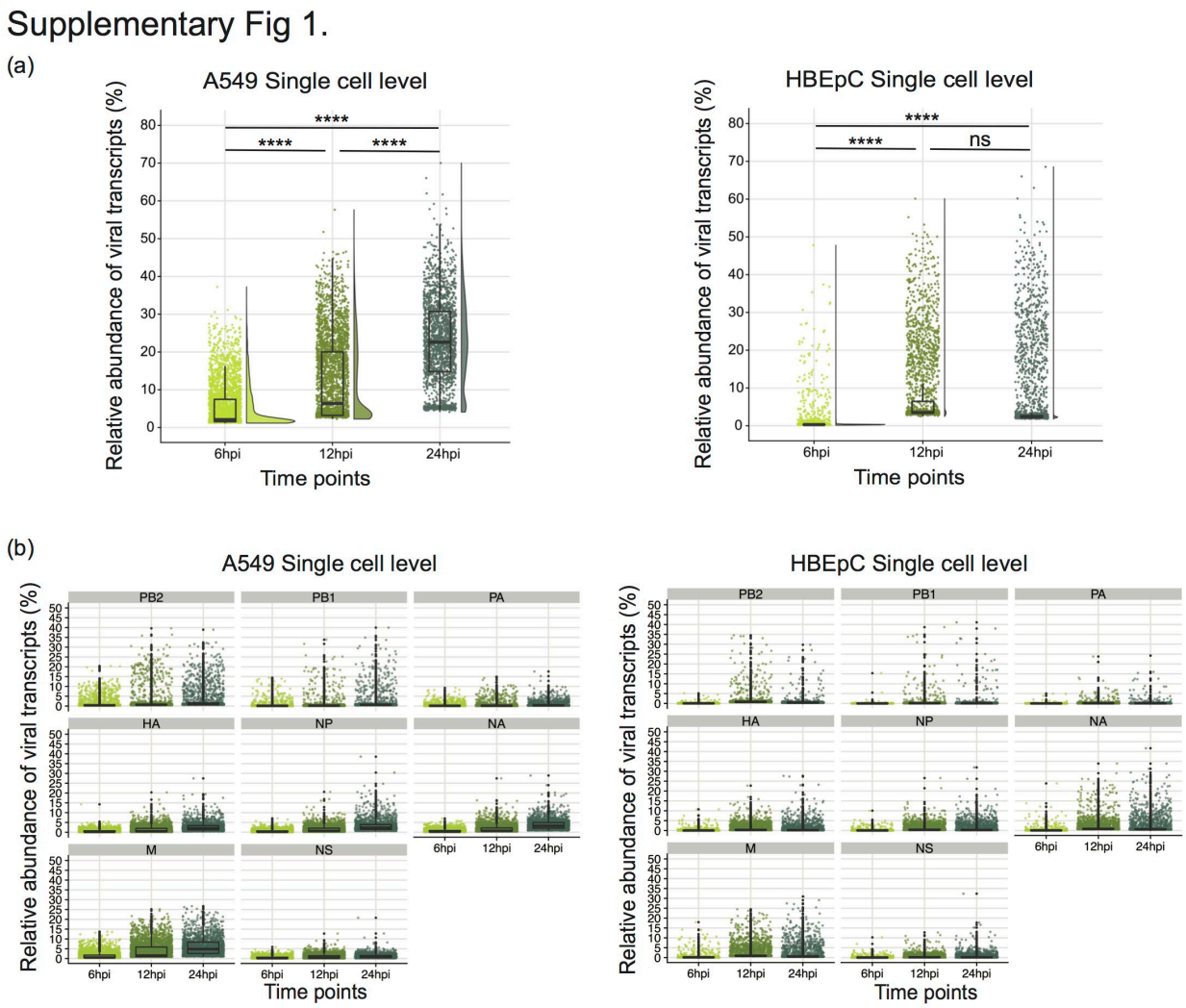

Supplementary Figure 1. Distribution of the relative abundance of viral transcripts within individual cells over the course of the infection. **(a)** The overall relative abundance of viral transcripts was calculated as the percentage of viral reads in the pool of all the reads for each cell. The dots are colored by the time points. All pairwise comparisons were performed with one-tailed Wilcoxon rank sum test, for which the null hypothesis was that cells harvested at an earlier time point have a lower median relative abundance of viral transcripts than those harvested at a later time point. The significance levels were denoted by the asterisks: * $p \leq 0.05$, ** $p \leq 0.01$, *** $p \leq 0.001$, **** $p \leq 0.0001$, and "ns" as not significant. The data for HBEpC cells

813 at 12hpi was collected from a repeated infection assay, due to the initial failure of single-cell
814 library preparation for the corresponding sample. **(b)** Distribution of the relative abundance of
815 viral transcripts derived from each segment within individual cells over the course of the
816 infection. All box plots show the first and third quantiles as the lower and upper hinges, the
817 median in the center, and 1.5 * inter-quartile range (IQR) from the first and third quantiles as the
818 whiskers.

Supplementary Fig 2.

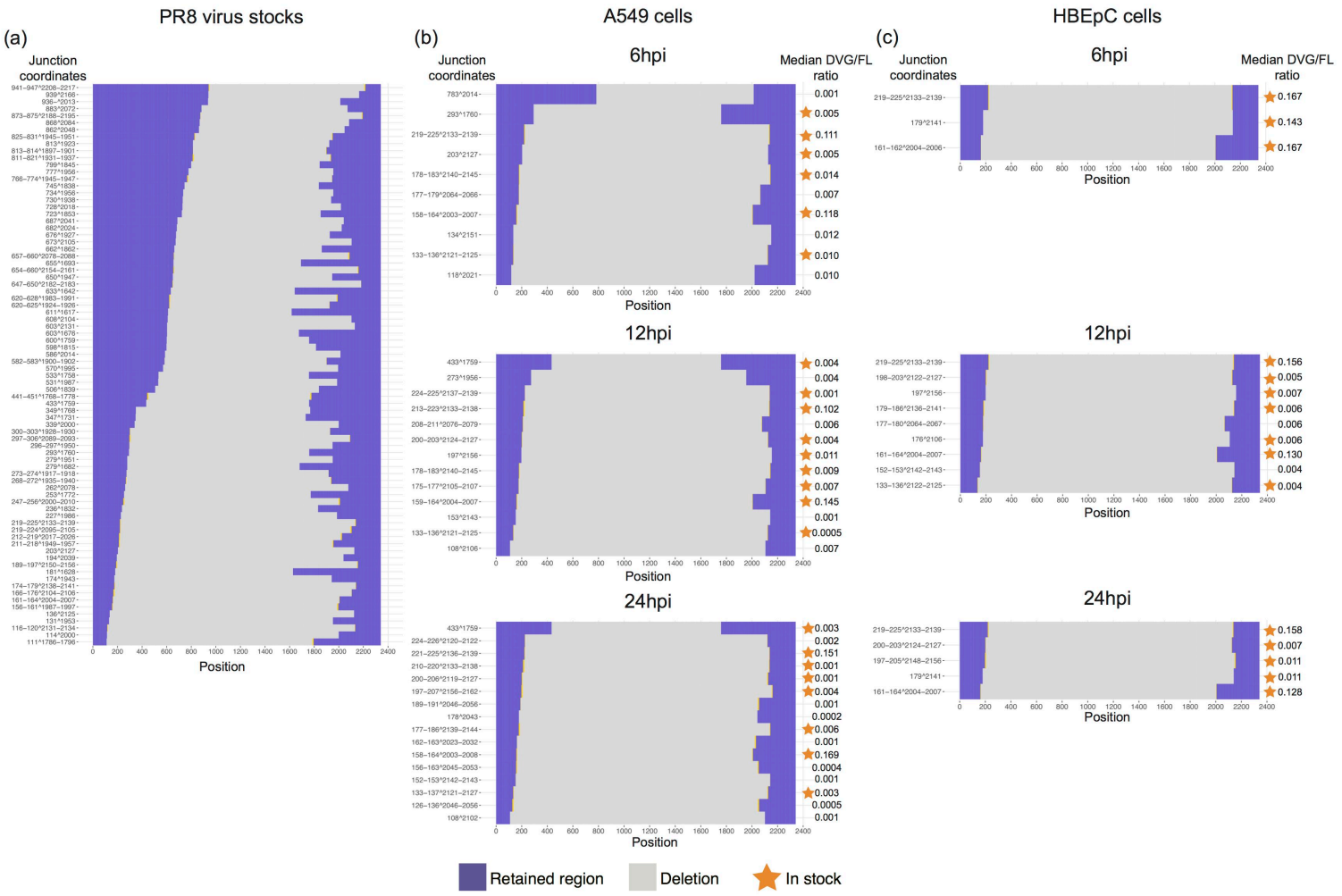

819

820 **Supplementary Figure 2.** Distribution of junction sites in the PB2 segment and the medians of their DVG/FL ratio in cells where a

821 given defective viral transcript was detected. **(a)** The defective PB2 segments detected in the PR8 virus stock used for infection. **(b-c)**

822 The DVG PB2 transcripts detected in **(b)** A549 and **(c)** HBEpC cells over the course of the infection. Transcripts carrying the same
823 junction sites as seen in the virus stock were denoted by asterisks.
824

Supplementary Fig 3.

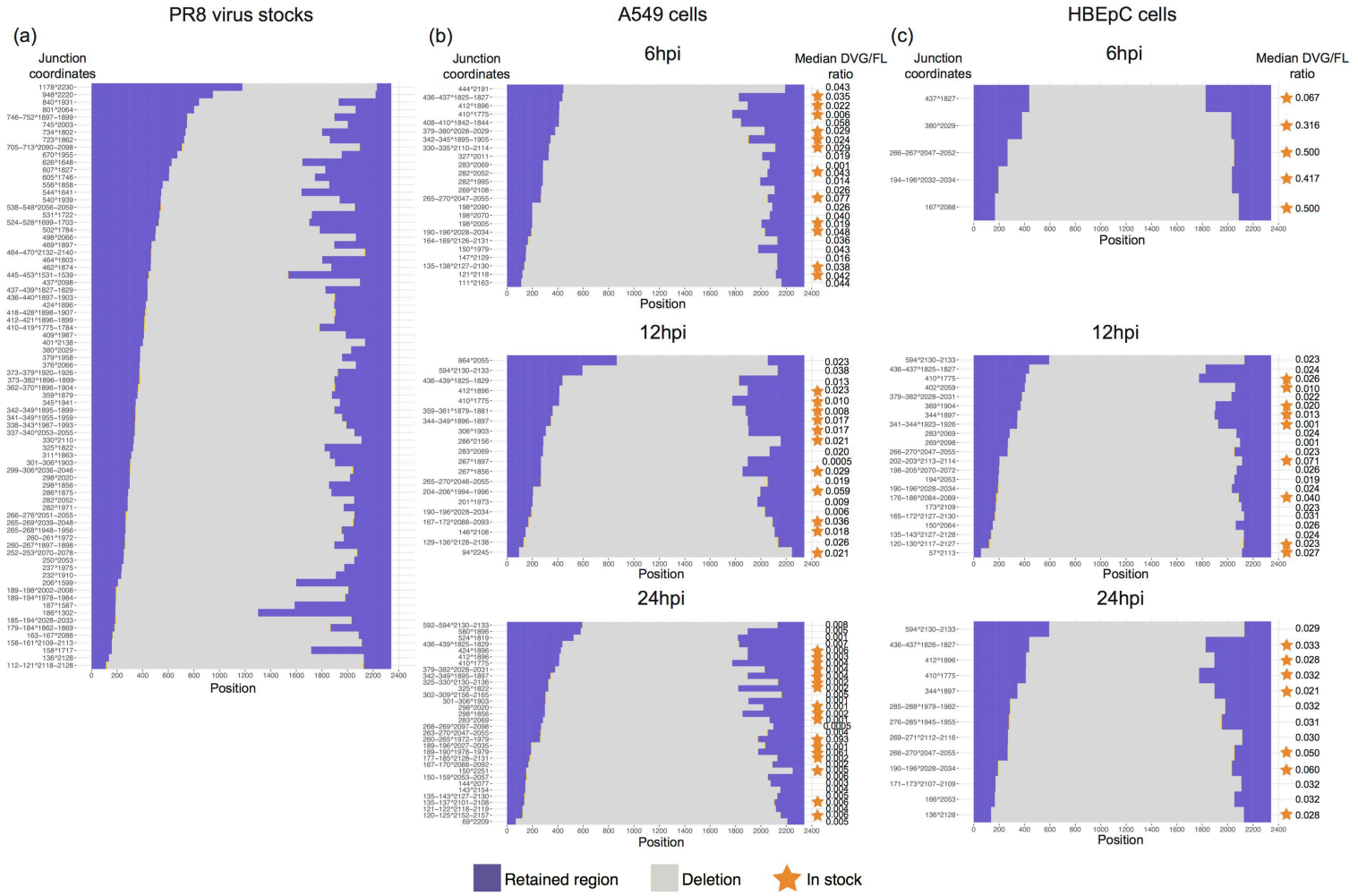

825

826 **Supplementary Figure 3.** Distribution of junction sites in the PB1 segment and the medians of their DVG/FL ratio in cells where a

827 given defective viral transcript was detected.

Supplementary Fig 4.

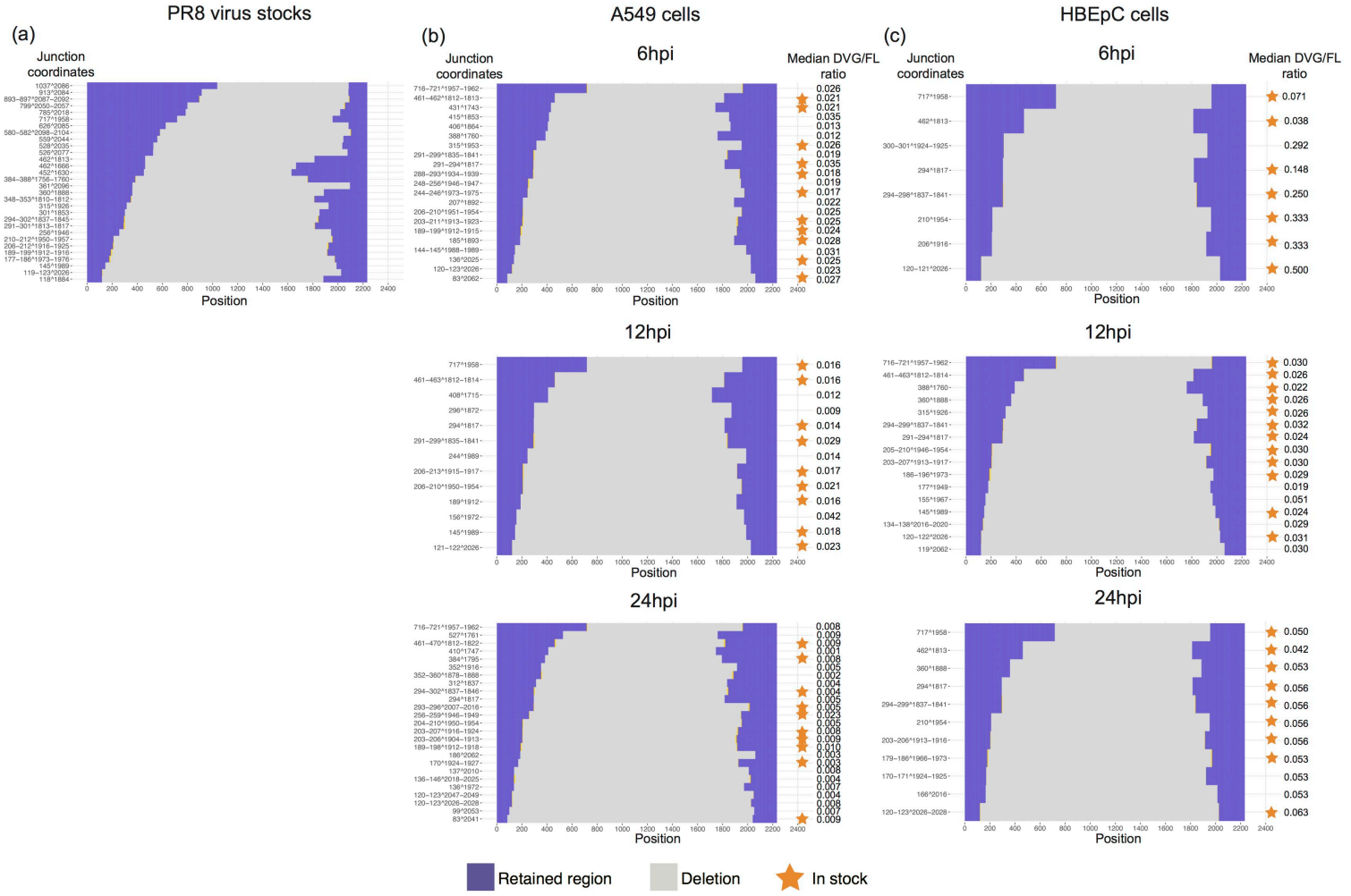

828

829 **Supplementary Figure 4.** Distribution of junction sites in the PA segment and the medians of their DVG/FL ratio in cells where a

830 given defective viral transcript was detected.

Supplementary Fig 5.

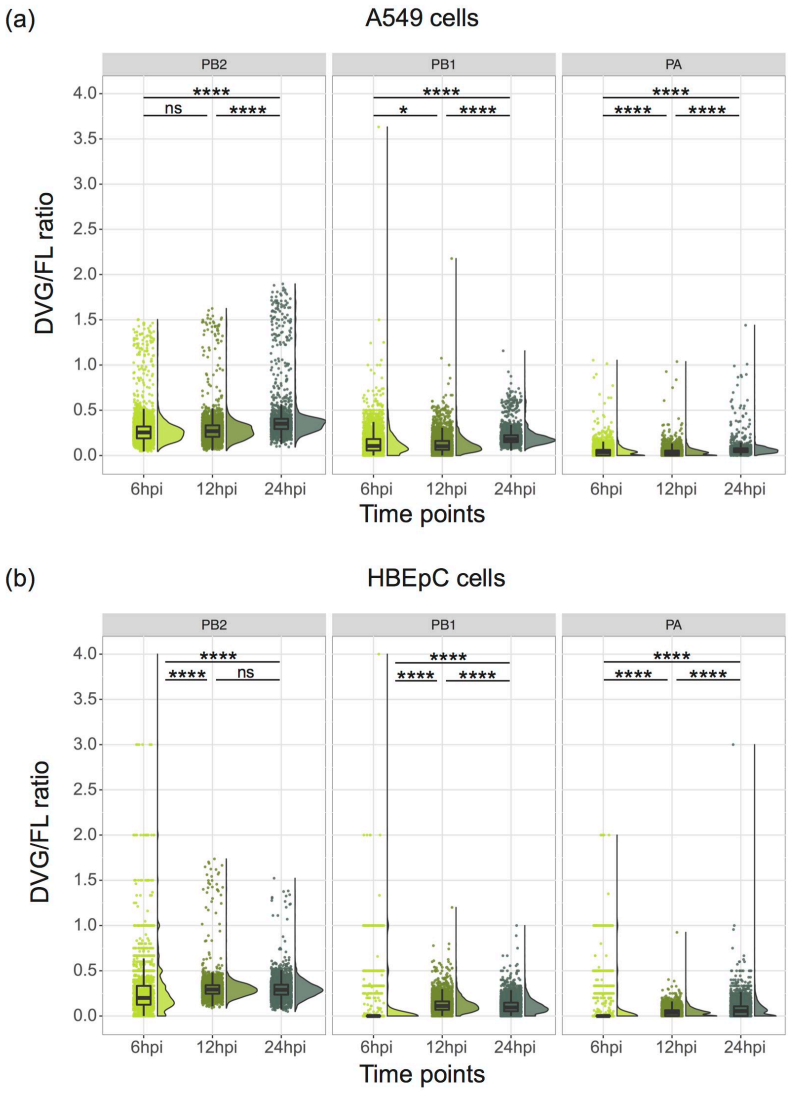

Supplementary Figure 5. Distribution of the DVG/FL ratio in A549 and HBEPC cells over the course of the infection. All pairwise comparisons were performed with two-tailed Wilcoxon rank sum test, for which the null hypothesis was that cells harvested at two different time points have different median relative abundance of viral transcripts. The significance levels were denoted by the asterisks: * $p \leq 0.05$, ** $p \leq 0.01$, *** $p \leq 0.001$, **** $p \leq 0.0001$, and "ns" as not significant. All box plots show the first and third quantiles as the lower and upper hinges, the median in the center, and 1.5 * inter-quartile range (IQR) from the first and third quantiles as the whiskers.

Supplementary Fig 6.

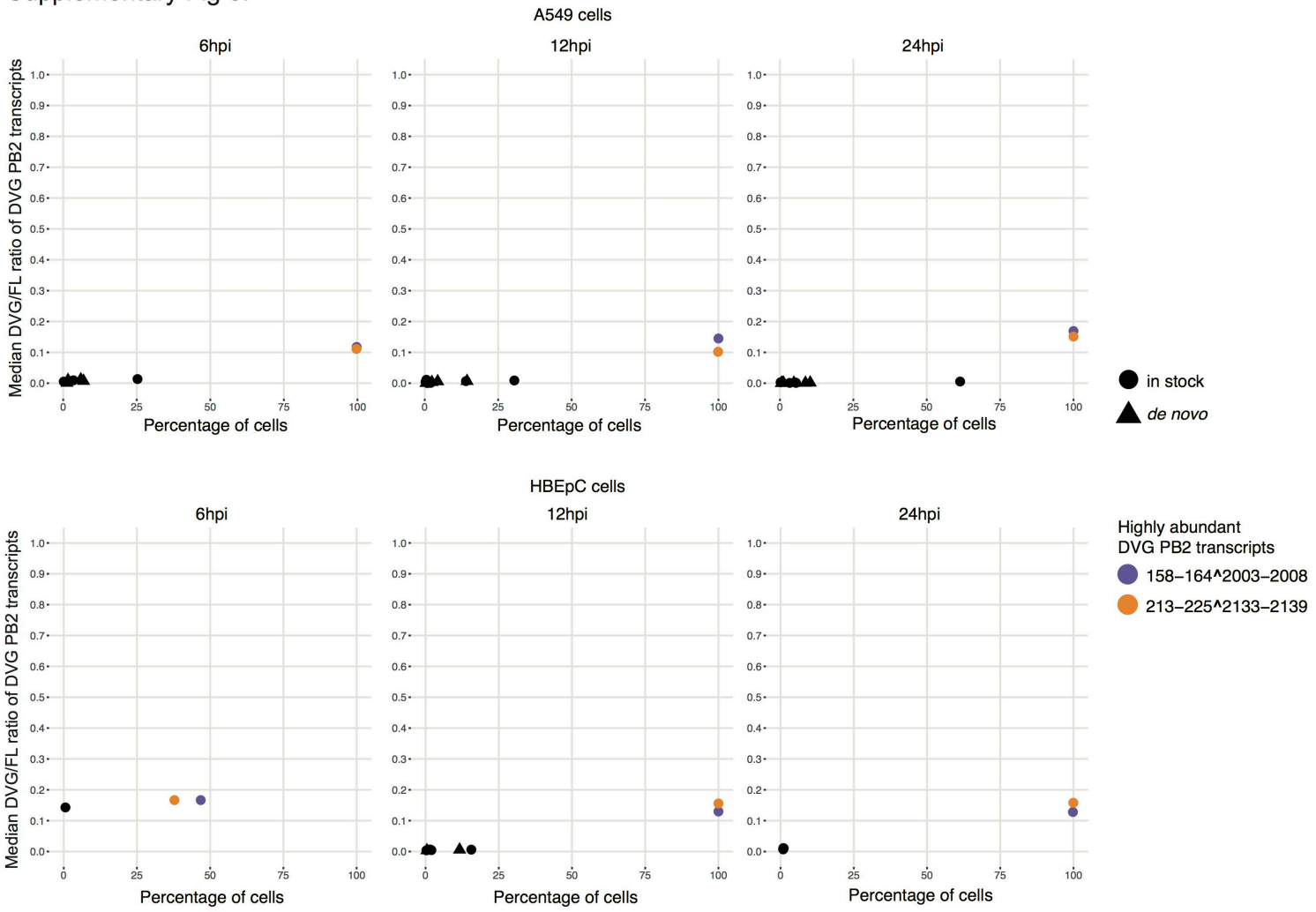

839

840 **Supplementary Figure 6.** Percentage of A549 and HBEpC cells in which a given DVG PB2 transcript was detected versus the

841 median of the DVG/FL ratio for that transcript in those cells over the course of the infection. Each type of DVG PB2 transcript was

represented by a dot or triangle. A dot denoted the DVG transcripts also seen in the virus stock and a filled triangle denoted the *de novo* generated transcripts. Two dominant DVG PB2 species were highlighted in slate blue and orange.

Supplementary Fig 7.

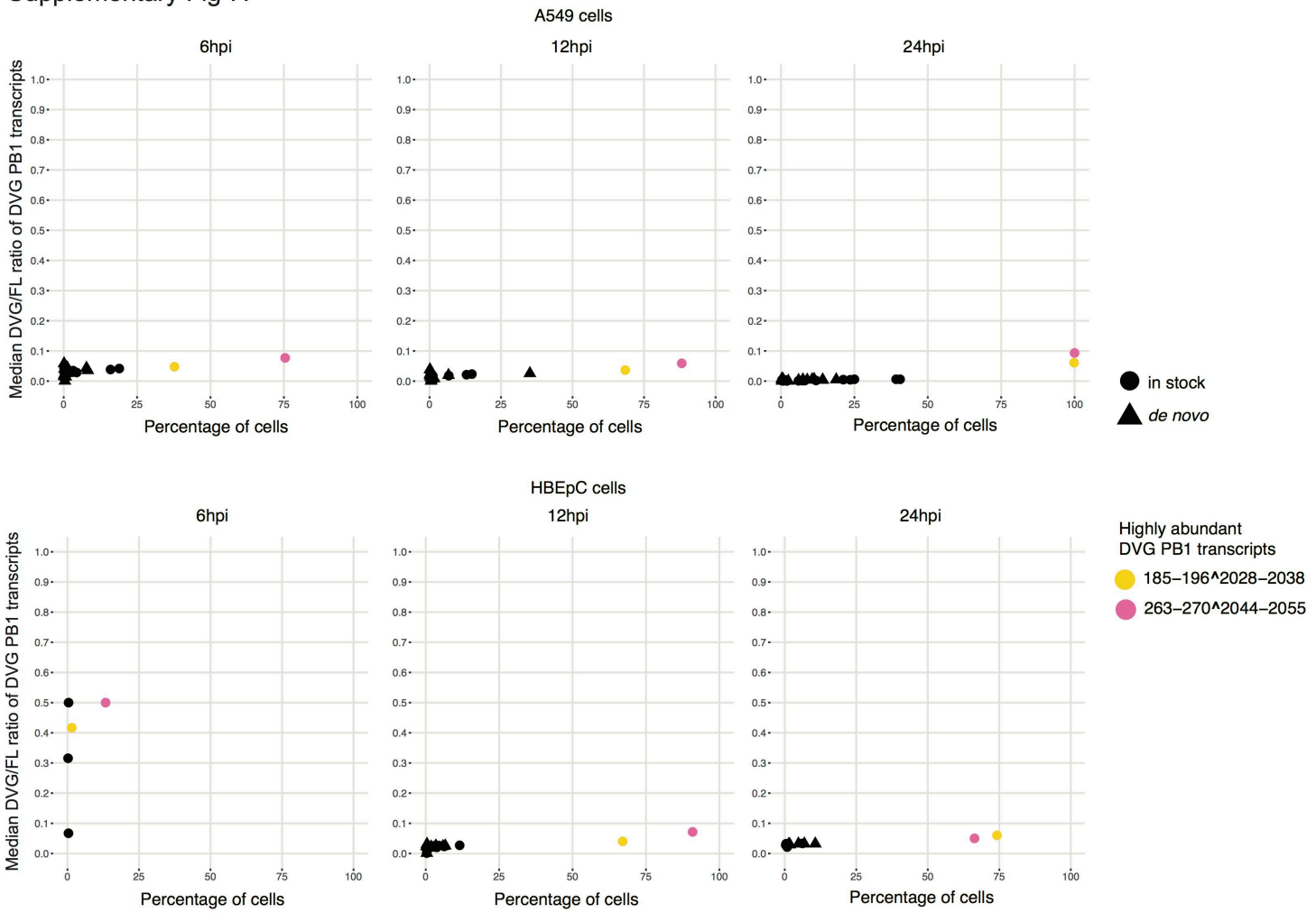

845

846 **Supplementary Figure 7.** Percentage of A549 and HBEpC cells in which a given DVG PB1 transcript was detected versus the
847 median of the DVG/FL ratio for that transcript in those cells over the course of the infection. Two dominant DVG PB1 species were
848 highlighted in yellow and pink.

Supplementary Fig 8.

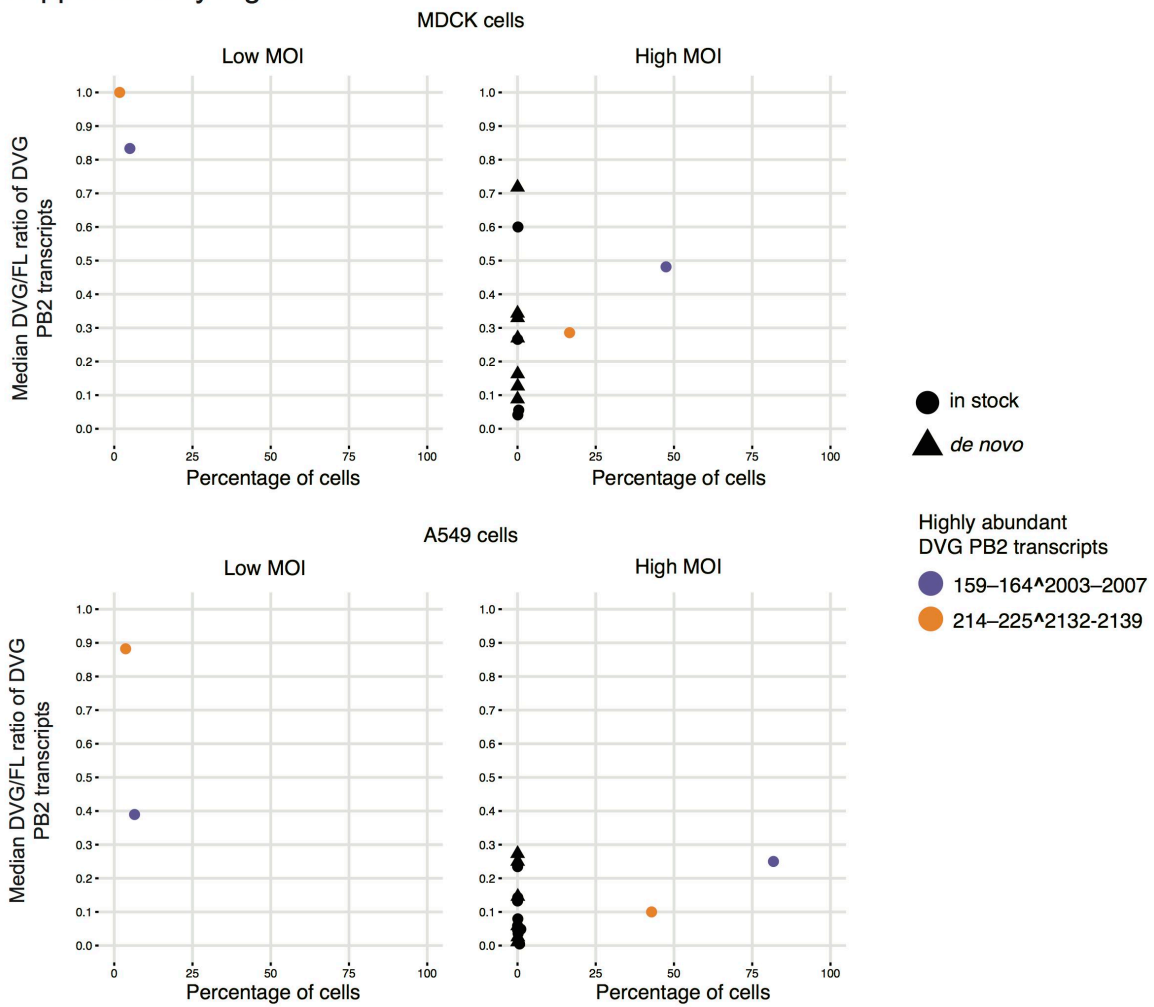

Supplementary Figure 8. Percentage of MDCK and A549 cells in which a given DVG PB2 transcript was detected versus the median of the DVG/FL ratio for that transcript in those cells. MDCK and A549 cells were infected with the same PR8 virus stock at

high (5) or low (0.2) MOI and harvested at 6hpi followed by 10X Genomics 3' single-cell library preparation and sequencing. Two dominant DVG PB2 species were highlighted in slate blue and orange.

Supplementary Fig 9.

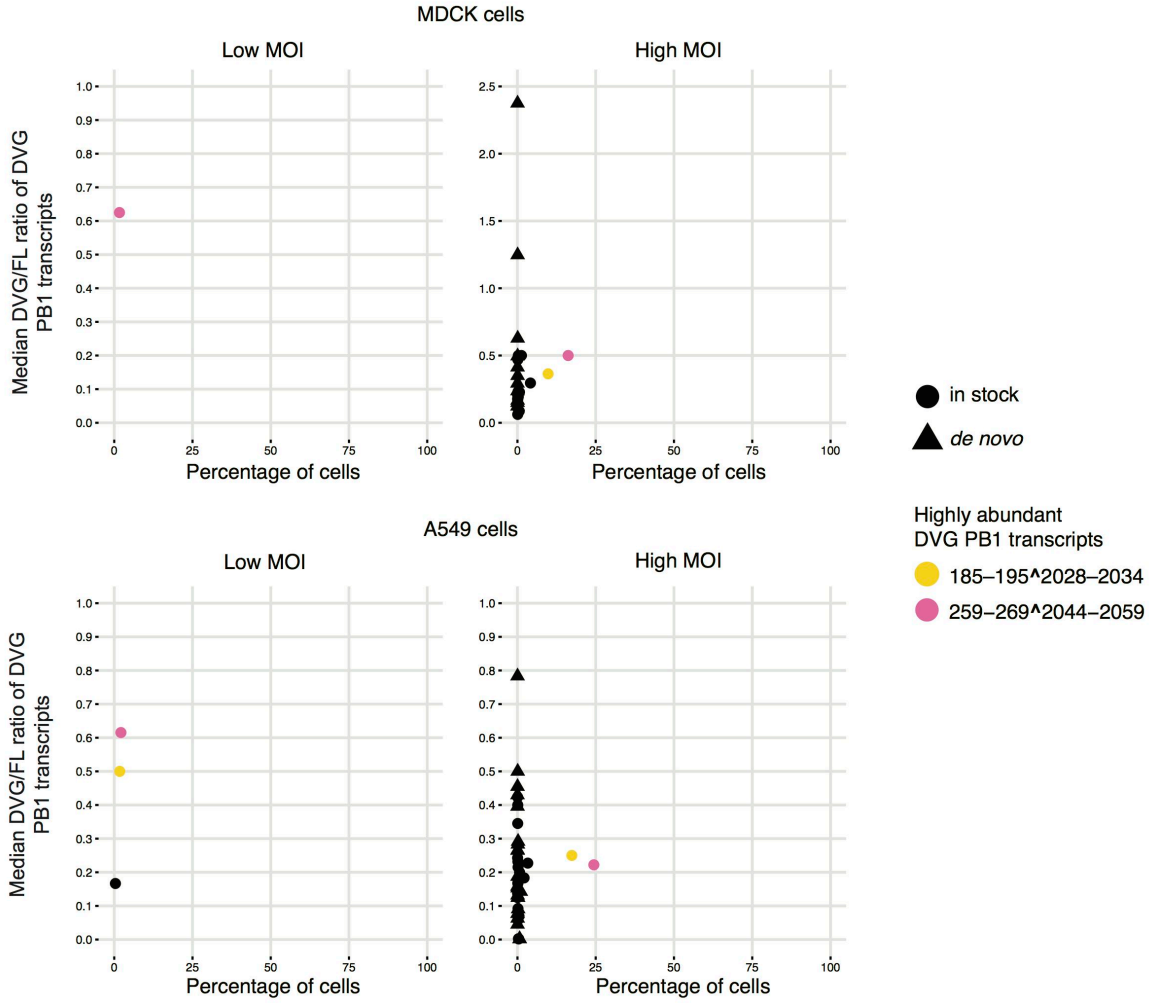

855

856 **Supplementary Figure 9.** Percentage of MDCK and A549 cells in which a given DVG PB1 transcript was detected versus the

857 median of the DVG/FL ratio for that transcript in those cells. MDCK and A549 cells were infected with the same PR8 virus stock at

high (5) or low (0.2) MOI and harvested at 6hpi followed by 10X Genomics 3' single-cell library preparation and sequencing. Two dominant DVG PB1 species were highlighted in yellow and pink.

Supplementary Fig 10.

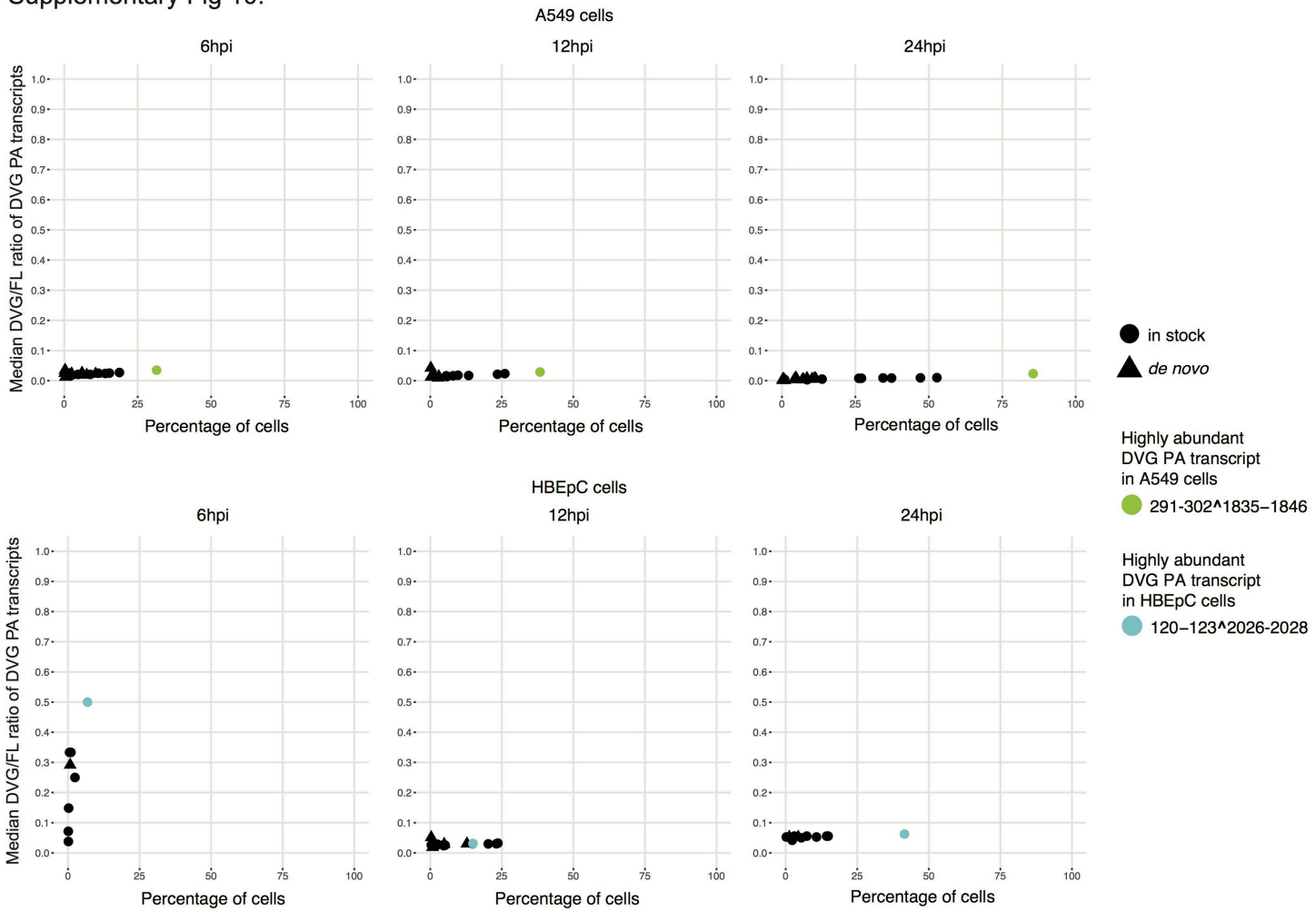

Supplementary Figure 10. Percentage of A549 and HBEpC cells in which a given DVG PA transcript was detected versus the median of the DVG/FL ratio for that transcript in those cells over the course of the infection. The dominant DVG PA species in each cell type were highlighted.

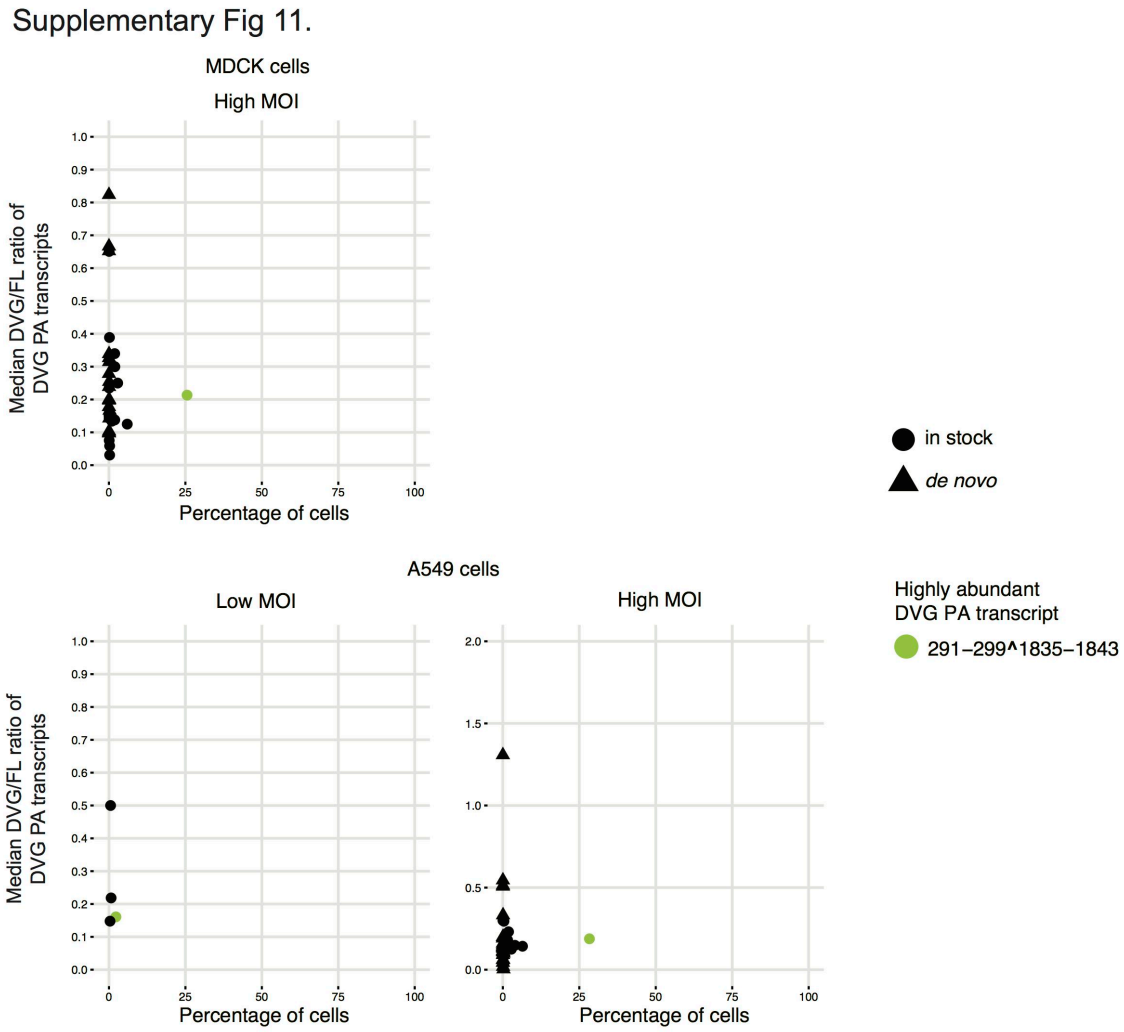

865

866 **Supplementary Figure 11.** Percentage of MDCK and A549 cells in which a given DVG PA transcript was detected versus the
867 median of the DVG/FL ratio for that transcript in those cells. MDCK and A549 cells were infected with the same PR8 virus stock at
868 high (5) or low (0.2) MOI and harvested at 6hpi followed by 10X Genomics 3' single-cell library preparation and sequencing. The

DVG PA transcripts were not detected in MDCK cells infected at low MOI. The dominant DVG PA species was highlighted in chartreuse.

Supplementary Fig 12.

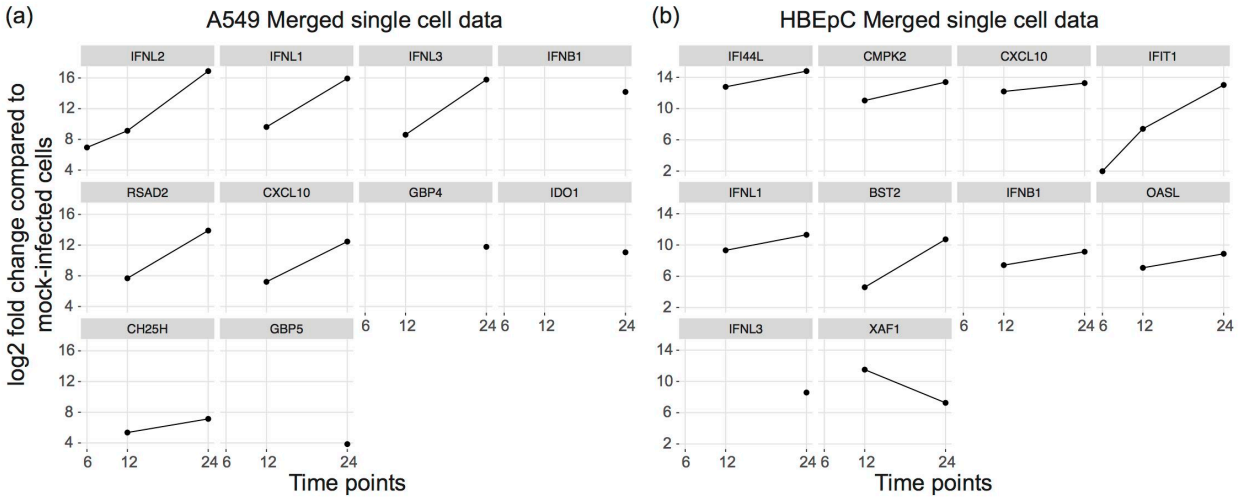

871

872 **Supplementary Figure 12.** The log2 fold change of the top 10 differentially expressed genes

873 identified at the bulk level in merged single-cell data that mimics the bulk level measurements.

874 The results from edgeR are shown.

875

Supplementary Fig 13.

876

877 **Supplementary Figure 13.** Visualization of un-supervised cell clustering on a t-SNE plot for

878 mock-infected **(a)** A549 and **(b)** HBEpC cells and the distribution of cell-cycle within the

879 population at each time point in two cell types. Each dot represents a cell on the t-SNE plot.
880 Dots were colored by either the cluster identities for the mock-infected cells, or the cell-cycle
881 stages for mock- and PR8-infected cells. The cell-cycle stage was assigned to each cell based
882 on the expression level of a list of cell-cycle markers.
883

Supplementary Fig 14.

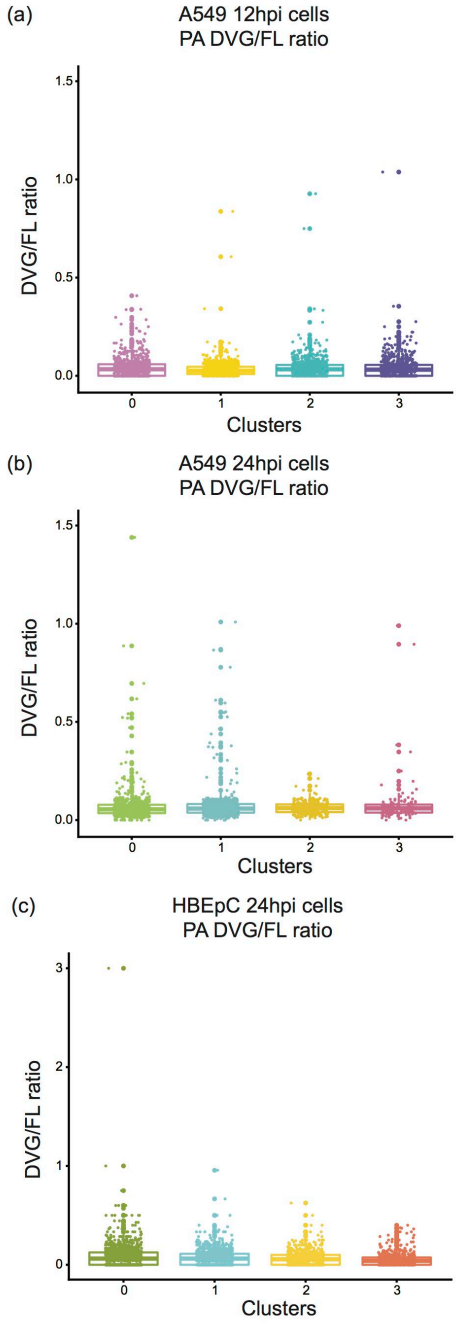

884

885 **Supplementary Figure 14.** Distribution of the DVG/FL ratio for the DVG PA transcripts in each
886 cluster of A549 cells at 12hpi and 24hpi and HBEpC cells at 24hpi. All box plots show the first
887 and third quantiles as the lower and upper hinges, the median in the center, and 1.5 * inter-
888 quartile range (IQR) from the first and third quantiles as the whiskers.

Supplementary Fig 15.

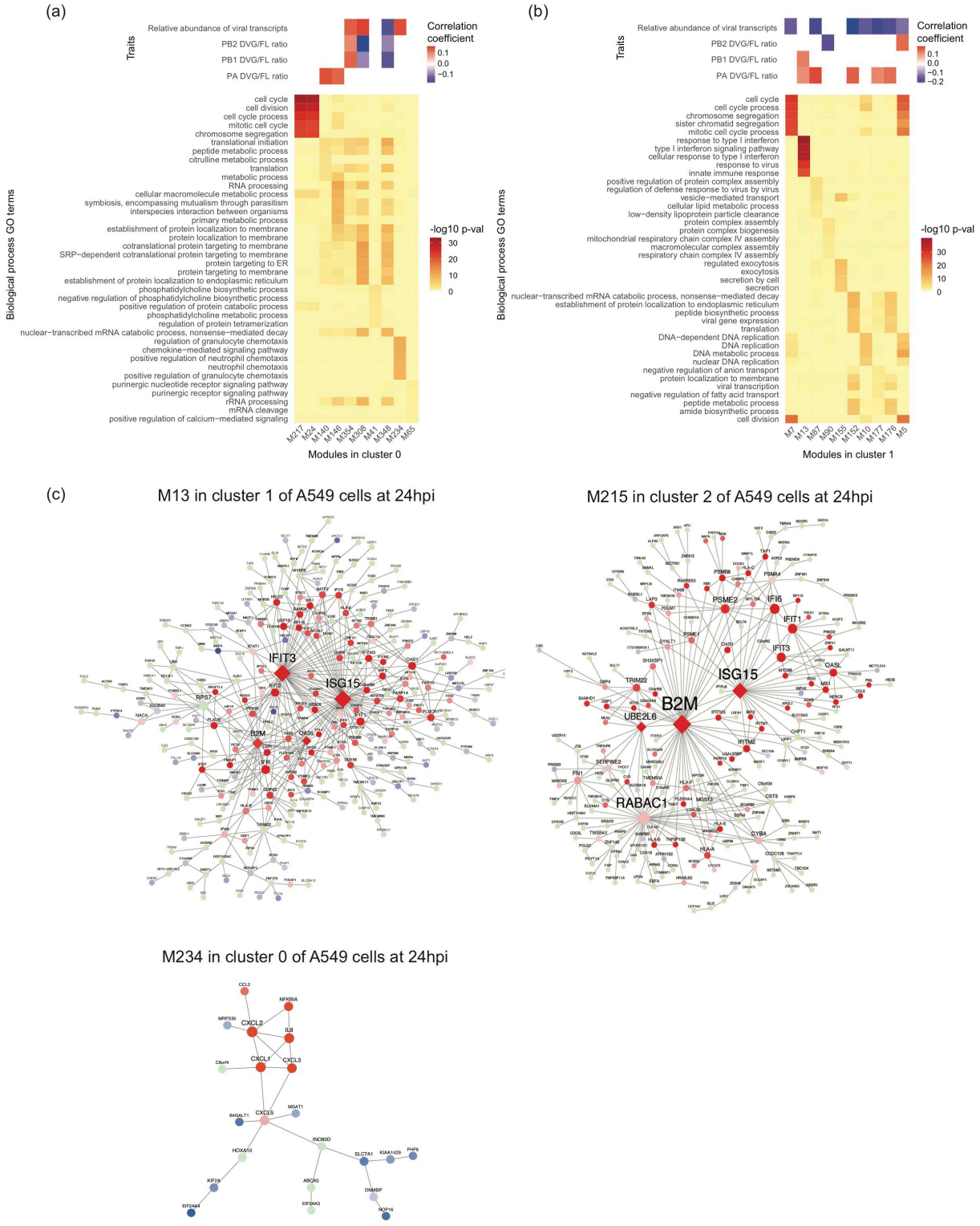

Supplementary Figure 15. Functional MEGENA modules in clusters 0 and 1 of A549 at 24hpi and networks revealing key regulators in modules enriched with innate immune response terms.

892 **(a-b)** Heatmaps of enriched biological process GO terms in the top 10 best ranked modules in
893 clusters **(a)** 0 and **(b)** 1 of A549 cells and the correlation between modules and the level of viral
894 transcription and DVG accumulation. Colors in the heatmaps of GO terms indicate FET p-values
895 after GO enrichment. Red and blue colors in the correlation heatmaps denote positive or
896 negative correlation with corresponding modules, respectively. **(c)** MEGENA network of
897 modules that are enriched for the innate immune response, including module M13 in cluster 1,
898 module M215 in cluster 2, and module M234 in cluster 0 of A549 cells. Red and blue nodes
899 represent significantly up- or down-regulated genes compared to all mock-infected cells, while
900 light-green nodes denote genes that are not significantly differentially expressed. Diamond
901 nodes indicate key regulators. The size of nodes indicates node strength after Multiscale Hub
902 Analysis within the MEGENA pipeline.
903

Supplementary Fig 16.

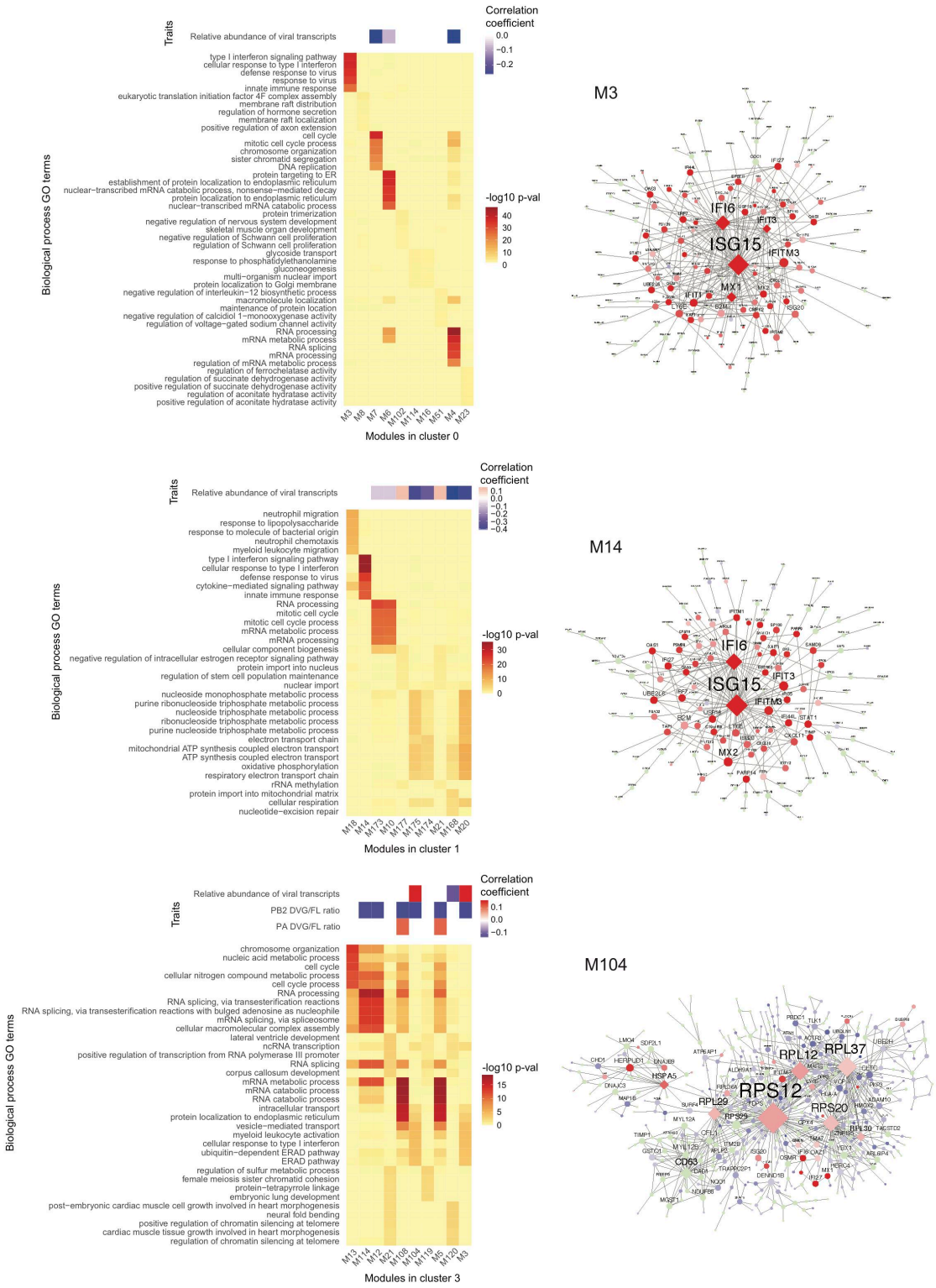

Supplementary Figure 16. Functional MEGENA modules in clusters 0, 1, and 3 of HBEpC at 24hpi and co-expression networks revealing modules enriched for type I IFN response. The left

907 panel shows the heatmaps of enriched biological process GO terms in the top 10 best ranked
908 modules and the correlation between modules and the level of viral transcription and DVG
909 accumulation. Colors in the heatmaps of GO terms indicate FET p-values after GO enrichment.
910 Red and blue colors in the correlation heatmaps denote positive or negative correlation with
911 corresponding modules, respectively. The right panel shows modules, including module M3 in
912 cluster 0, module M14 in cluster 1, and module M104 in cluster 3, enriched for type I IFN
913 response.
914

Supplementary Fig 17.

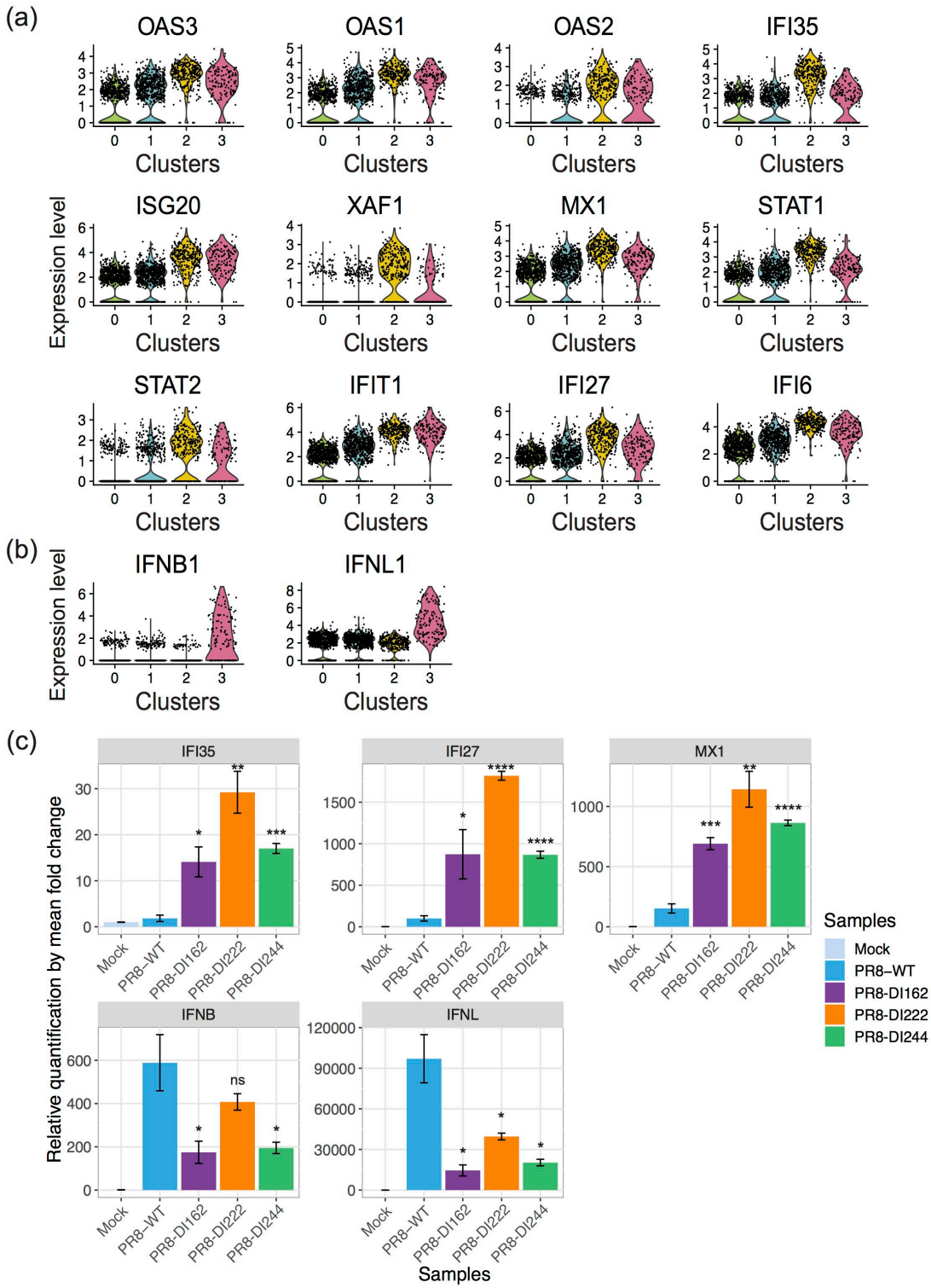

915

916 **Supplementary Figure 17.** Expression of ISGs and IFNs in DI-enriched A549 cells at 24hpi. **(a-**

917 **b)** The expression level of **(a)** significantly over-expressed genes in cluster 2, which are

associated with GO terms related to the type I IFN signaling pathway and have the fold change on the log-scale >= 1, and **(b)** type I and III IFNs, in each cluster of A549 cells at 24hpi. The dot represents the normalized expression level of a gene in each cell. The violin shade is colored by the cluster identity. **(c)** Validation of over-expression of selected ISGs and IFNs by qPCR. Subconfluent A549 cells were either mock-infected or infected with one type of PR8-DI virus (PR8-DI162, -DI222, or -DI244) or PR8-WT virus at a MOI of 10. Total RNA was extracted from cells collected at 24hpi. The levels of ISGs and IFNs mRNA were determined by qPCR and normalized to the level of β-actin (ACTB). The error bar representing the standard deviation of the mean was obtained from three biological replicates. Statistical tests were done using two-tailed Student's *t*-test in R to compare the differences in fold change between PR8-WT and PR8-DI infection. The significance levels were denoted by the asterisks: * $p \leq 0.05$, ** $p \leq 0.01$, *** $p \leq 0.001$, **** $p \leq 0.0001$, and "ns" as not significant.